Linking persistent scatterers to airborne laser scanning points for identifying real objects reflecting SAR signal

Wielgocka, Natalia; Jóźków, Grzegorz; van Leijen, Freek; Hanssen, Ramon; Pawluszek-Filipiak, Kamila

DOI
10.1515/jag-2024-0084

Publication date
2025

Document Version
Final published version

Published in
Journal of Applied Geodesy

Citation (APA)
Wielgocka, N., Jóźków, G., van Leijen, F., Hanssen, R., & Pawluszek-Filipiak, K. (2025). Linking persistent scatterers to airborne laser scanning points for identifying real objects reflecting SAR signal. *Journal of Applied Geodesy*. https://doi.org/10.1515/jag-2024-0084

Natalia Wielgocka*, Grzegorz Jóźków, Freek van Leijen, Ramon Hanssen and Kamila Pawłuszek-Filipiak

Linking persistent scatterers to airborne laser scanning points for identifying real objects reflecting SAR signal

https://doi.org/10.1515/jag-2024-0084
Received September 25, 2024; accepted April 30, 2025;

Abstract: The Persistent Scatterers Interferometry (PSI) method enables displacement estimation with millimeter accuracy. However, the uncertain positioning of Point Scatterers (PS) makes it difficult to associate them with real objects in space and hampers the interpretation of the results. This article proposes a methodology to enhance the accuracy of PS positions. The methodology successfully establishes links between PS and real objects by associating them with the most likely candidate points extracted from Airborne Laser Scanning (ALS) point clouds. The selection process for suitable candidates is based on ALS analysis of return number, classification, and geometric features determined by neighborhood analysis. The linking process involves determining global transformation parameters for PSs using the Iterative Closest Point (ICP) algorithm. Then, the nearest neighbor search within the error ellipsoid of the PS positions is performed. Tests conducted demonstrated that this method allows for linking more than 80 % and 65 % of the PS derived from Sentinel-1 and TerraSAR-X mission data, respectively, in both ascending and descending geometries. To validate the obtained results, in addition to the quantitative assessment, a qualitative analysis is performed based on a developed 3D visualization module showing all stages of the proposed methodology.

Keywords: airborne laser scanning; persistent scatterers interferometry; data fusion

1 Introduction

Persistent Scatterers Interferometry (PSI) is one of the advanced multi-temporal Interferometric Synthetic Aperture Radar (InSAR) methodologies based on the analysis of time series of satellite radar images [1]. PSI estimates the surface displacement using phase observations from selected coherent points called Persistent Scatterers (PSs). Stack-based processing is crucial for eliminating the residual topographic error and atmospheric artifacts, resulting in highly precise displacement estimates at the millimeter level [2], thereby overcoming the limitations of traditional Differential InSAR (DInSAR). For this reason, it is widely used to measure surface displacement caused by various phenomena, such as earthquakes [3], landslides [4, 5], volcanic eruptions [6], city developments [7, 8], and mining activities [9, 10]. Another popular multi-temporal InSAR technique, the Small Baseline Subset (SBAS), allows the analysis of displacements for individual SAR pixels, which contain a group of smaller reflectors named distributed scatterers. PSI focuses on point targets representing objects with high stability in reflected signals, characterized by high coherence [11]. For this reason, PSs are typically found in large numbers on buildings, monuments, and man-made structures, such as bridges, telecommunication towers, poles as well as conductors, and exposed rocks. Thus, this technique is mainly used to estimate displacement in urban areas [12] and for infrastructure monitoring like roads [13], railways [14], and bridges [15] as well as single buildings [16]. Thanks to the capability to monitor vast regions with high temporal resolution and high accuracy, the PSI processing results have recently been presented on various regional and national services

---

***Corresponding author: Natalia Wielgocka**, Institute of Geodesy and Geoinformatics, Wrocław University of Environmental and Life Sciences, Grunwaldzka 53, 50-375 Wrocław, Poland,
E-mail: natalia.wielgocka@upwr.edu.pl.
https://orcid.org/0000-0002-8420-7046
Grzegorz Jóźków and Kamila Pawłuszek-Filipiak, Institute of Geodesy and Geoinformatics, Wrocław University of Environmental and Life Sciences, Grunwaldzka 53, 50-375 Wrocław, Poland.
https://orcid.org/0000-0003-4953-9253 (G. Jóźków),
https://orcid.org/0000-0003-2162-371X (K. Pawłuszek-Filipiak)
Freek van Leijen and Ramon Hanssen, Department of Geoscience and Remote Sensing, Delft University of Technology, Stevinweg 1, Delft, 2628CN, The Netherlands.
https://orcid.org/0000-0002-2582-9267 (F. van Leijen),
https://orcid.org/0000-0002-6067-7561 (R. Hanssen)

such as European Ground Motion Service (EGMS) [17], German Ground Motion Service (BodenBewegungsdienst Deutschland – BBD, https://bodenbewegungsdienst.bgr.de) and the Dutch Ground Motion Service (https://bodemdalingskaart.nl).

However, PSs suffer from poor position accuracy, meaning that it is challenging to associate them with real objects [18]. The precise position of a point and its association with objects in space is a crucial aspect that facilitates result interpretation. Firstly, knowing the object from which the signal originates allows for interpreting displacement mechanisms. When multiple forcing mechanisms are involved, establishing a correlation between persistent scatterers and specific objects is particularly important. For instance, observed displacements may result from a combination of both structural instability and deep-layer compaction processes [19]. Secondly, the exact location of a point on a specific object enables the identification of structures behaving differently. Thirdly, more accurate PS position and additional information about the source object of the scatterer can enhance the quality of the deep-learning models, which are more and more often implemented in InSAR data processing [20, 21] in recent years. Moreover, aligning with real-world objects in 3D can be leveraged when preparing visualizations of the obtained results on different platforms that showcase InSAR processing outcomes. Currently, many of these services rely on two-dimensional maps, such as an orthophoto, where the assumption is that the PS originates from a visible object on the map base.

The technique that allows the mapping of objects with high accuracy and spatial resolution is Light Detection and Ranging (LiDAR). Depending on the scanning technique, such as Airborne Laser Scanning (ALS), UAV-borne Laser Scanning (ULS), Mobile Laser Scanning (MLS), or Terrestrial Laser Scanning (TLS), the point cloud density, area coverage, and accuracy will vary. Nevertheless, ALS technology makes it possible to acquire accurate geometric data about the terrain of a large area in a short period. Additionally, for many countries, ALS is conducted nationwide, and in some cases, the data is freely available. Therefore, this data can provide a way of reference for the position of the PS in three-dimensional space. The integration of the PSI processing with the LiDAR point cloud will be beneficial in improving the accuracy of the position of the PS and, thus, a more precise interpretation of the obtained displacement results. The concept of a high-resolution ALS point cloud to improve the accuracy of PS positions has been addressed in the literature [22], but in our opinion, there is still a possibility to improve the accuracy. Therefore, in this paper, we propose a new approach for improving the localization of PSs in reference to ALS point cloud and, consequently, more links of PSs to real objects represented by ALS points. The novelties of our contribution are:

- A multi-step ALS point pre-selection algorithm, which takes the nature of the radar signal reflection into account;
- Treating the PS points as a point cloud to determine the global transformation parameters (both translation and rotation in 3D space) using the Iterative Closest Point (ICP) algorithm.

This paper is structured as follows. Section 2 reviews, in general, other works that addressed the problem of improving the position of the PS. Section 3 describes the proposed methods and experiment setup. In Section 4 used data are presented. The results obtained are given in Section 5 and discussed concerning the results of other studies in Section 6. Finally, conclusions are drawn in Section 7.

2 Related work

PS position accuracy is affected by many factors, which can be divided into four main groups [23]: (1) radar satellite instrument effects, (2) signal propagation effects, (3) geodynamic effects, and (4) coordinate transformation effects. Improving PS positioning accuracy is a widely studied topic in the scientific community because the precise location of the estimated PS significantly impacts the interpretation of the obtained displacements for a specific object. Therefore, many different approaches to PS localization accuracy have been developed in the last few years. The first group includes corrections to PS position in the radar coordinate system, i.e., range and azimuth. These corrections reduce the impact of errors such as azimuth shift, atmospheric path delay, plate motion, and solid earth tides [24–26]. However, these methods do not consider the cross-range position, which affects the PS position in the 3D terrain coordinate system. Usually, these approaches compare results obtained for corner reflectors (CRs), easily identified in the radar image and for which a well-defined scattering center is measured accurately using Global Navigation Satellite Systems (GNSS) techniques or a total station.

A second group of approaches attempted to use a kind of ground control point (GCP), widely used in photogrammetry, to determine offsets between the position of a potential scattering source and estimated PS. For example, studies [16, 27] aimed to use identical objects for which PS was obtained in different imaging geometries (orbits) to obtain accurate 3D terrestrial coordinates of the scatterers.

Typically, these are narrow objects such as poles. However, the primary drawback of this method, especially for medium- and low-resolution (C-band and L-band) SAR products, is the small number of detected GCPs. Therefore, this method is most suitable for urban areas where there are a lot of PS and appropriate objects. Additionally, for lower-resolution SAR products, GCP identification could be more challenging, especially when the study area has a high density of such structures.

On the other hand, in ref. [28] the authors used CRs as GCP to improve positioning accuracy through three approaches: single-epoch, multi-epoch, and artificial GCP derived from digital surface models. The first two methods require access to CRs and field measurements, while the third method allows for accuracy improvement based solely on free-available data without additional field measurements. However, the proposed methods are based on determining global transformation parameters. Thus, in practice, they do not allow the linking of each PS to the real object but only to improve the accuracy of the position relative to it.

In the study conducted by Van Natijne et al. [22], an innovative approach was introduced, allowing each PS to be linked individually to the LiDAR point cloud. The linking is carried out inside the PS position error ellipsoid, which is a graphical representation of the variance-covariance matrix of the PS position [23]. Reference [29] adopts a similar method for monitoring displacements in railway areas and PS classification. Searching for candidates to merge inside the PS error ellipsoid seems to be a valid approach. Points inside the ellipsoid are more likely to be the source of PS than the nearest point in 3D space. On the other hand, this approach relies solely on the geometric alignment of PS data to LiDAR without incorporating the physical properties of radar measurements. Study [30] used a different approach, incorporating 3D city models in Level of Detail 1 and 2 standards (LOD1 and LOD2) and ray tracing to simulate radar signal propagation. They aimed to identify the true PS within the error ellipsoid for each simulated point, achieving 10 % and 37 % data matching with the TerraSAR-X PS dataset for LOD1 and LOD2, respectively. The low matching percentage is due to the significant shape generalization of individual buildings. This highlights the challenges of accurately simulating PS data within the context of 3D city models and ray tracing. However, in ref. [31], the authors did not consider the PS position uncertainties and focused solely on individual buildings. They performed clustering of PS points based on the behavior of time series and connected them with building segments derived from manually segmented mesh.

The PSI processing also impacts the accuracy of the PS position. In recent years, numerous AI (artificial intelligence) based modifications to the PSI processing methods have been proposed. The shallow and deep learning-based methods have been proposed to enhance traditional PSI processing results through phase denoising [32], phase unwrapping [33], and target detection for densification of the generated PS [33]. While these methods enhance the estimated displacements in both qualitative and quantitative terms, they come with their own set of challenges. One major limitation is that deep learning models require substantial amounts of training data, which can be labor-intensive and time-consuming to prepare. Additionally, while these methods enhance displacement accuracy, they do not address the positional accuracy of persistent scatterers, making the problem of assigning PSs to real objects still unsolved.

Thus, considering the ongoing need to improve the PSs position accuracy and linking them to real objects, we decided to use the ALS point cloud as a reference object and search for the closest points in the error ellipsoid. Our approach does not require CR or field measurements, and the only condition is the availability of ALS data, which may have been acquired for other purposes and are often available in national resources. We aim to demonstrate that by utilizing simple and widely known tools, without the laborious process of preparing data for deep learning, we can enhance the accuracy of PS position and their correspondences to real objects. The most important aspect of this work is to select suitable candidates in the LiDAR data and link the PS that are nearby to them. To accomplish this, we pre-selected the ALS cloud and pre-corrected the PS position using ICP to determine the global transformation parameters between the PS and LiDAR clouds.

3 Methods

The method of PS geolocalization correction consists of four main steps (Figure 1), described in detail in the following subsections. The first step is the estimation of PS position uncertainties based on PSI processing results (Section 3.1). The second step, which can be executed in parallel with the first step, is LiDAR point cloud processing (Section 3.2). The third step is the co-registration of PS points and LiDAR point cloud using the ICP algorithm (Section 3.3). The final linking of PSs with particular LiDAR points is described in Section 3.4. In addition, the results were validated both quantitatively as well as qualitatively where a 3D visualization module was implemented to visualize and assess linking results (Section 3.5).

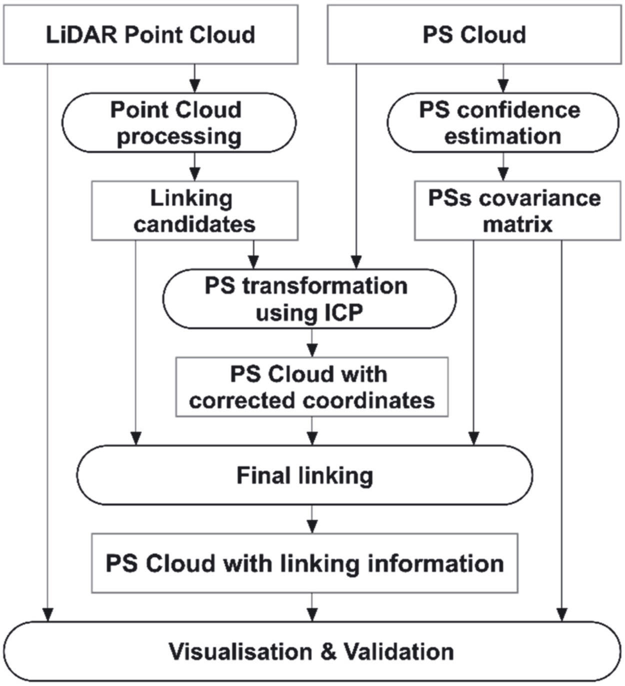

Figure 1: PS linking methodology flowchart.

All computations and the visualization module have been implemented in Python, utilizing various libraries, such as GDAL (https://gdal.org/), GeoPandas (https://geopandas.org/), NumPy (https://numpy.org/) [34], Open3d (http://www.open3d.org/), and PyVista (https://docs.pyvista.org/).

3.1 Point scatterer position uncertainty

Persistent Scatterer Interferometry is a widely adopted advanced InSAR technique for displacement monitoring with millimeter-level accuracy [35, 36]. Numerous studies provide a comprehensive discussion of PSI processing details [1, 11, 37, 38]. In this section, we will focus on the methodology involved in estimating the position uncertainty of PSs.

In the radar coordinate system, the position of a scatterer is defined in range (r), azimuth (a), and cross-range (c) coordinates. Range refers to the direction of the radar signal, azimuth to the direction of the satellite's flight, whereas cross-range is perpendicular to the range and azimuth direction. Range and azimuth can be estimated from the mean of the full stack of SAR images by detecting the effective phase center of the radar scatterer. The units of the estimates used are pixels. The variances (σ^2) of point scatterer (P) position in azimuth and range directions are dependent on the signal-to-clutter ratio (SCR_P), which describes the uncertainty of the peak position caused by clutter or the presence of more than one dominant scatterer, and oversampling factor Δ_P [23]:

$$\sigma^2_{r,P} = \sigma^2_{a,P} = \frac{3}{2 \cdot \pi^2 \cdot SCR_P} + \frac{1}{12\Delta^2_P}. \tag{1}$$

In this study, the SCR_P was calculated in the same manner as in ref. [29] using the normalized amplitude dispersion index. In addition, since no oversampling of the data was applied, an oversampling factor equal to 1 was used to calculate the scatterer variances for the range and azimuth coordinates.

In order to estimate the cross-range variance, InSAR observations are required. According to previous studies [23, 29] the variance of P position along the cross-range direction was calculated by transforming the height variance ($\sigma^2_{h,P}$) to the radar geometry (azimuth, range and cross-range) by using the following equation:

$$\sigma^2_{c,P} = \frac{\sigma^2_{h,P}}{\sin^2(\theta)}, \tag{2}$$

where θ is the incidence angle.

The uncertainty of the scatterer position in the radar geometry can then be described using the following variance-covariance matrix (Q_{rac}):

$$Q_{\text{rac}} = \begin{bmatrix} \sigma^2_{r,P} & 0 & 0 \\ 0 & \sigma^2_{a,P} & 0 \\ 0 & 0 & \sigma^2_{c,P} \end{bmatrix}. \tag{3}$$

The Q_{rac} matrix is diagonal because it is assumed that the range, azimuth and cross-range coordinates are uncorrelated. The PS position in the radar coordinate system is transformed to a geodetic reference frame by a non-linear transformation called geocoding [27]. Then, coordinates can be transformed into a specific coordinate system, e.g., to the system in which LiDAR data are provided. This means that the position uncertainty in the reference coordinate system depends on the range, azimuth, and cross-range uncertainties, as well as the local incidence angle and heading angle of the radar signal that affects the transformation parameters. Considering the variance propagation law and Equation (3), using an S-transformation matrix (R) [23, 39], the variance-covariance matrix in the geodetic reference frame is given by [23]:

$$Q_{enh} = \begin{bmatrix} \sigma^2_e & \sigma^2_{en} & \sigma^2_{eh} \\ \sigma^2_{en} & \sigma^2_n & \sigma^2_{nh} \\ \sigma^2_{eh} & \sigma^2_{nh} & \sigma^2_h \end{bmatrix} = R \cdot Q_{\text{rac}} \cdot R^T, \tag{4}$$

where the diagonal and nondiagonal represent the variances and covariances in east (e), north (n), and height (h) directions, respectively. The R matrix is defined based on the radar's geometry, incorporating the local incidence angle (θ) and heading angle (α):

$$R = \begin{bmatrix} \sin(\theta)\cos(\alpha) & \sin(\alpha) & \cos(\theta)\cos(\alpha) \\ -\sin(\theta)\sin(\alpha) & \cos(\alpha) & -\sin(\alpha)\cos(\theta) \\ -\cos(\theta) & 0 & \sin(\theta) \end{bmatrix}. \quad (5)$$

The geometric representation of the variance-covariance matrix Q_{enh} is an error ellipsoid with semi-axis lengths equal to the eigenvalues of the Q_{enh} matrix. These values reflect the random errors in the positions of PSs. Effects of systematic errors causing misalignment of PS positions with reference frame are reduced at the transformation stage using the ICP algorithm (Section 3.3).

3.2 LiDAR point cloud processing

Among the LiDAR techniques mentioned earlier (Section 1), ALS appears to be particularly suitable for the problem discussed because it can cover large areas, and its acquisition geometry is similar to SAR. Compared to PSs, ALS data has a denser point distribution and higher point position accuracy. However, a drawback of ALS is the relatively low number of points on building facades, especially in urban canyons. This limitation poses a challenge when attempting to capture intricate urban structures.

In this study, we assumed that ALS and PS can be the same points, though LiDAR and SAR use different wavelengths and different principles of signal reflection and point creation. C-band and X-band SAR signals can penetrate some objects (e.g., vegetation, snow) to some extent depending on the wavelength (longer wavelengths enable deeper penetration). However, such surfaces generally do not generate PSs because they cannot be classified as stable scatterers. The penetration for more solid surfaces is negligible, considering the accuracy of ALS points. ALS uses typically infrared wavelength that, in general, does not penetrate objects, causing points to be created on the object surfaces with the single laser pulse. Because the laser beam is divergent, parts of the pulse footprint may "fall" on different objects (e.g., different parts of the tree, ground) producing multiple echoes of the single laser pulse. This multiple return capability of the ALS causes an illusory effect of vegetation penetration, but points are always created on the top of the surfaces.

Most PSs are related to man-made structures because of their strong scatterer mechanism [40], while ALS data contains points that also belong to other objects. ALS points are usually assigned to real objects thanks to classification into typical point classes defined by ASPRS standard [41]. However, some ALS point classes may contain a mixture of objects suitable and unsuitable for PS forming. Therefore, appropriate ALS data filtering is crucial to minimize the risk of linking PSs to LiDAR points that are not PSs. The selection of appropriate linking candidates from the ALS point cloud is essential at two distinct processing stages: firstly, during the position correction utilizing ICP, and secondly, in the final linking stage (Figure 1). The proposed method involves a few simple filters (Figure 2) that significantly limit the number of wrong PSs candidates in the ALS dataset. In this research, we propose a filtering workflow that, besides the information about existing classification, considers echo number and geometrical features of points that can distinguish some of man-made objects and considers side-looking SAR geometry.

The first step of the proposed filtering workflow is ALS point filtering based on the echo information, which is a feature of pulsed scanners exclusively utilized in ALS [42]. In our method, we keep only points being the first echo since PSs cannot be created on the ground surface or other objects under vegetation cover. The second stage contains normal vector and point feature calculation using Principal Component Analysis (PCA). The normal vector is used during ICP registration and for point cloud filtering in specific class similarly as linearity and planarity features. The proposed method can be applied to any laser scanning as well as photogrammetry point cloud that has at least 3 classes: Ground (natural and man-made), Buildings (containing roofs and walls), and Unclassified (all remaining points). Classes Ground and Buildings contain objects that create most of the PSs. The remaining points may be included in the Unclassified class or may belong to other classes. If any other class exists in the ALS dataset, it can be one of three types: (I) completely removed from PS candidate search (e.g., classes: Vegetation, Water, Low points), (II) completely accepted as PS candidates (e.g., Infrastructure class), (III) additionally filtered to search for possible PS candidates similarly as Unclassified class. The class Buildings follows additional filtering to remove points that stay in the shadow due to the SAR satellite line of sight (LOS). Considering the necessity to filter only two classes: Unclassified and Buildings, among the possible PCA-based features, three parameters were used: planarity, linearity, and information about surface orientation (normal vector). For the reliable determination of these features, choosing an appropriate point neighborhood for applying PCA and calculating these features is crucial. As an optimal neighborhood, the authors in ref. [43] defined the largest set of spatially close points

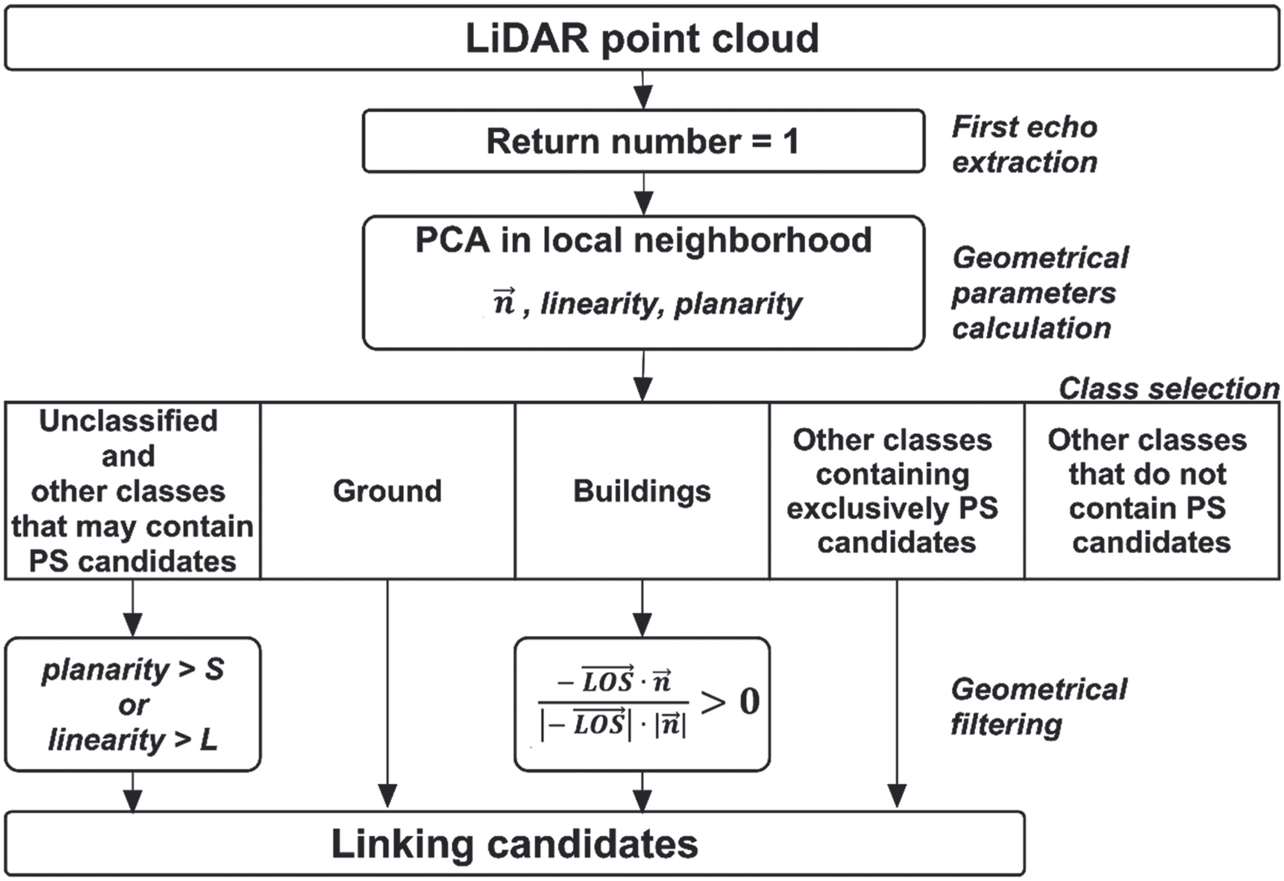

Figure 2: Methodology LiDAR point cloud filtering for PS linking candidate selection.

that belong to the same object as the point of interest. According to ref. [44], the optimal number of points in the neighborhood that provides the best local description of the point cloud for different classes of objects is 10 points. The neighborhood size should be large enough to enable PCA feature determination for all points of the tested objects while being small enough to prevent the inclusion of points from neighboring objects in the defined local neighborhood. Among the methods for finding neighboring points, a spherical neighborhood was used, with the radius determined experimentally. The tested radius range was 0.5–3.0 m and resulted from the density of the ALS point cloud. The value of the final radius was determined based on tests conducted on ALS points representing several man-made linear objects (such as poles and fences) and planar objects (such as sound barriers and information boards) that can form PS.

The selection of potential PS candidates, being infrastructure objects but located in the Unclassified class, is dependent on planarity or linearity values. Points exceeding predefined S or L thresholds (Figure 2) are accepted as potential PS candidates. For instance, utility poles and cables would exhibit high linearity values, while sound barriers or fences would display elevated planarity values. Natural objects are less likely to meet the specified criteria. Thresholds for S and L were determined empirically by analyzing the abovementioned test objects. The maximum values that ensured all test objects were classified as potential PS candidates were selected as the appropriate thresholds. A set of S and L values from 0.5 to 0.9 with a step of 0.05 were tested. The maximal value of 0.9 was taken based on the literature [45]. The final stage of the proposed PS candidate filtering methodology is intended to remove points from the Buildings class that are in the shadow with respect to the SAR imaging geometry. Due to the significant differences in geometry between SAR and ALS, this step addresses the fact that SAR is a side-looking system, whereas LiDAR captures data from a top-down perspective. This difference can addressed by the SAR signal incidence angle to the object surface (e.g., building façade, roof, etc.). For this purpose, the angle between each point's normal vector and the vector opposite the LOS of the radar signal is computed. Points with an angle larger than 90° are identified as in shadow and then removed. The LOS-opposite vector is calculated as a unit vector based on angles describing the LOS geometry

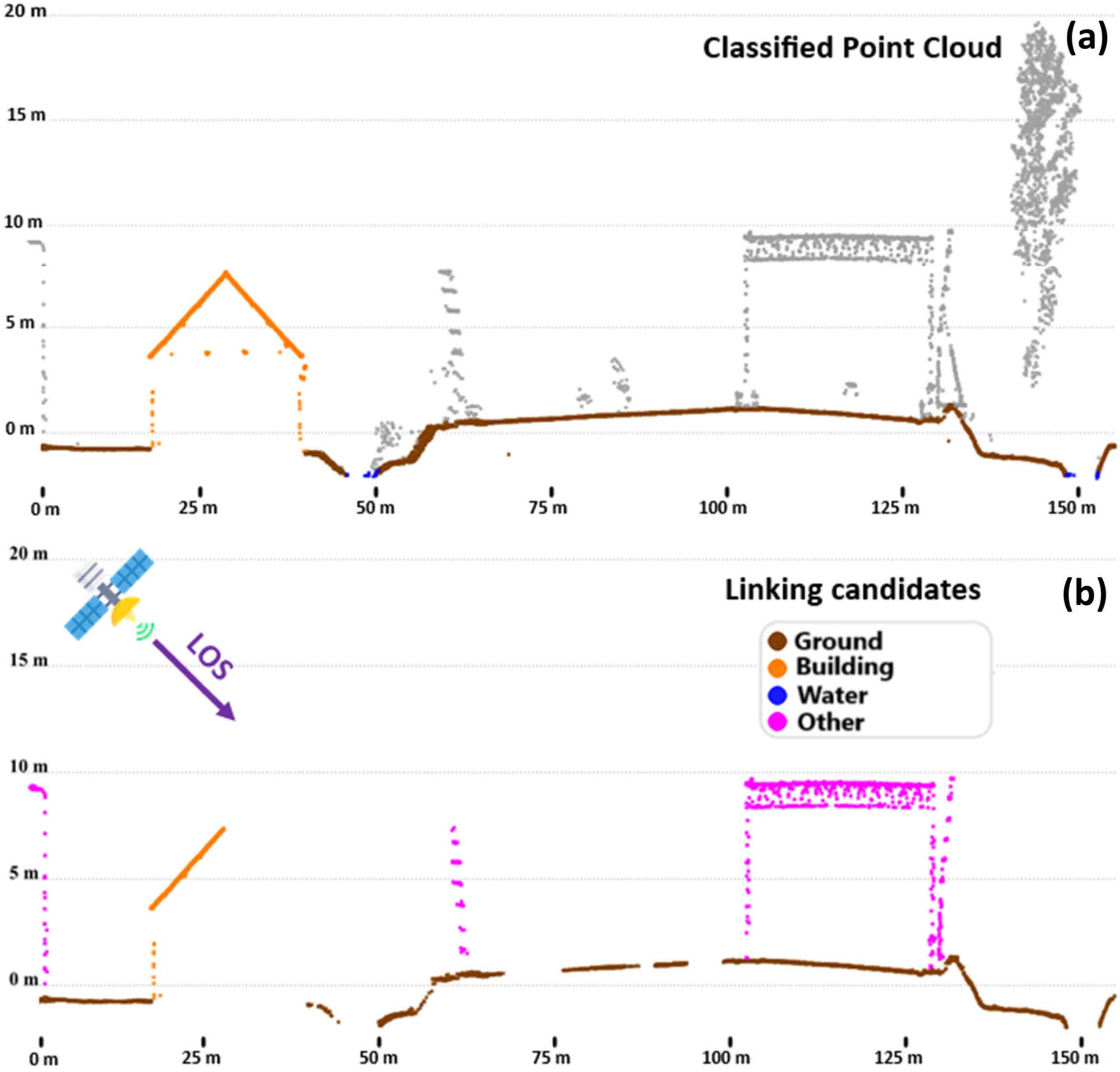

Figure 3: PS candidate selection methodology. (a) Shows the cross-section of original ALS data and the main classification of the point cloud. (b) Presents the results of the proposed methodology.

– the azimuth and incidence angle. The final result of the filtering method is illustrated in Figure 3.

3.3 Global transformation parameters estimation using Iterative Closest Point algorithm (ICP)

In radar geometry, the position of PS can be influenced by various factors, which can be categorized into two main groups: systematic factors applicable to the entire dataset and factors specific to a particular PS point. Systematic offsets are caused by, e.g., SAR image timing errors, orbit errors, uncompensated atmospheric signal delays, and a PS reference point height offset. The additional individual PS point position errors are due to uncertainty in the scatterer peak detection (SCR dependent) and the PS height estimate. Using a LiDAR point cloud as well as other datasets such as surface models, it is possible to reduce the effect of errors. In ref. [29] authors proposed an iterative procedure to eliminate systematic height shifts using a gridded surface model obtained by LiDAR data. This method is more precise than single-point correction but does not estimate all shifts independently. In this work, we suggest estimating not only shifts between PSs and LiDAR point clouds but also rotations. We propose to treat the PSs as a sparse point cloud and execute point cloud-to-point cloud registration using the well-known ICP algorithm, which allows the transformation that optimally aligns two or more sets of points. The ICP algorithm has many implementations and modifications aimed at improving its accuracy. During the optimization process in the ICP algorithm, the goal is to minimize the distance between a point in the transformed cloud and a point in the target cloud. This distance minimization can involve point-to-point, point-to-line, or point-to-plane relationships, depending on the specific problem configuration. In this research, we used the point-to-plane distance minimization criteria in the ICP algorithm implementation included in the Open3D Library for Python [46]. Our study focuses on ALS point clouds, where, due to the scanning geometry, low point density on a vertical wall is often a challenge. Therefore, using a point-to-plane approach seems to be an appropriate choice. The point-to-plane distance between two corresponding points is defined as the orthogonal distance of one point to the fitted plane of the other point [47]. The plane for a point from the reference cloud is usually determined based on its neighboring points. In this work, we determined these planes in the previous step (Section 3.2) by calculating the normal vector for each point. Minimizing the distance determined in this strategy proves to be a helpful approach, particularly in situations characterized by areas of low point density. In such cases, the distance to the plane formed by the selected points is expected to be less than the slant distance to the actual point. In this research, as a target point cloud the ALS dataset after the PS candidate selection step was chosen. This is a crucial assumption because, in the ICP algorithm, the closest points are treated as corresponding points. Thus, ALS points that cannot correspond to PSs should be removed.

The ICP algorithm implementation used in this work has a few parameters that need to be provided: initial coarse transformation parameters, distance threshold, and convergence criteria. Initial coarse transformation parameters include rotation and translation parameters that describe the initial alignment of point clouds. Because PSs are transformed earlier from radar geometry to the geodetic frame of the LiDAR point cloud, both point clouds are in the same coordinate system. Thus, coarse transformation parameters are equal to 0. The distance threshold is the maximum point-to-plane distance accepted. The computations do not include points for which the distance threshold is exceeded. In this work, the distance threshold is set to equal the maximum pixel size in the radar geometry of the SAR image, i.e., 14 m and 2 m for Sentinel-1 and TerraSAR-X data, respectively. The convergence criteria decide when the iteration process ends. In this work, two parameters of convergence criteria were used: a maximum number of iterations of 100 iterations and a change in RMSE values between the two last iterations of smaller than 0.001 m. The RMSE is calculated from point-to-plane distances for inlier points that met the ICP threshold criteria. The iteration process ends when any of these criteria are met. The results of the executed ICP algorithm are the transformation parameters from PS to LiDAR point cloud and ICP quality assessment values. Estimated transformation parameters were applied to PS the point cloud, and thus, the corrected PS point cloud was prepared for final linking.

3.4 Final linking

Using the ICP method, it is possible to improve the accuracy of the position of PSs, but they are still not linked to real objects because the same translation and rotation value is applied to all points. Therefore, an individual approach to each point is required. For the final PS linking, we adopted the methodology proposed in ref. [22] involving a nearest neighbor search process concerning the radar geometry that links the scatterers to their most likely point in the LiDAR point cloud. Searching is performed inside the error ellipsoid defined by the variance-covariance matrix which was described in detail in Section 3.1. An error ellipsoid at the 2-sigma confidence level was used, meaning that the true reflection point is expected to be within the ellipsoid in approximately 95 % of the cases.

Since the original error ellipsoids based on Q_{rac} are typically non-spherical due to differences in the variances in the azimuth, range and cross-range directions, this also applies to the error ellipsoids after transformation. Consequently, finding the closest LiDAR point and, thereby, the most likely PS scatterer location is not straightforward. Therefore, a whitening transformation [48] is adapted to decorrelate the original data, providing a set of uncorrelated data with unit variances. The transformation matrix (W) is formed using the eigenvalues (E) and eigenvectors (D) of the covariance matrix of PS in the geodetic reference frame (Q_{enh}):

$$W = E^{-1}D^{-\frac{1}{2}}E^{T}. \tag{6}$$

A transformation was performed on the ALS and PS point clouds. After this transformation, searching the nearest neighbor in the LiDAR point cloud to each PS can be performed in the Euclidian space. The PS point was assigned with the selected LiDAR point coordinates (corrected position) and within the confidence ellipsoid. Otherwise, its PS position was not corrected. If the confidence ellipsoid contained more than one point, the selection of the single linking point was based on the point class and the distance to the ellipsoid center. The priority of links was put on the class Buildings, then Ground and Infrastructure (if it exists), and in the last order, the newly created Other class. The prioritization of classes was applied according to object type suitable to form PS and to prevent links to noise points that were not completely removed from the Unclassified class during filtering but are closer to the ellipsoid center than points from other classes. If more than one point of the same class was included in the confidence ellipsoid, the nearest neighbor to the ellipsoid center was selected as the PS link.

The final output of the entire linking procedure is the original PS dataset enriched with corrected PSs coordinates obtained during final linking, the LiDAR-based class assigned to the PSs, and information regarding the determined variances in the radar geometry. PS points not linked to LiDAR points did not get corrected coordinates and class.

3.5 Validation

3.5.1 Quantitative evaluation

The validation of the 3D linking accuracy should be based on an assessment of the accuracy of associations with objects that actually reflect the signal. In particular, for targets with known effective phase centers such as CRs, the true reflection center is well known, and it can be measured on-site using e.g., GNSS [49]. Unfortunately, these objects are rarely or never available in certain scenarios, such as for our test sites. Following the approach proposed in ref. [23], validation in scenarios without CR targets involves establishing connections with real-world objects as non-CR targets. This validation approach quantifies the number of links with these non-CR targets. The percentage of points at which a linking procedure discovers a new position on a real object has been used several times in the literature to evaluate the quality of linking [22, 29, 30, 50]. In some cases, depending on the particular application in which linking was used, the authors focused only on the classes of interest to them [51]. In this contribution, we also consider the percentage of successfully linked PSs as a metric to assess the quality of the proposed approach. The performance of the proposed method was also validated by analyzing the percentage of linked PSs and their assignment to a particular class for the method that excludes one of the proposed key steps: (1) removing systematic errors using the ICP algorithm and (2) filtering of ALS points. The lower number of linked PSs, their assignment to classes that cannot create PSs (e.g., vegetation), or significant differences in percentage for the PS obtained from different orbits will indicate lower performance. Note that the percentage ratio of PSs assigned to a particular class should be similar for descending and ascending orbit datasets within the same satellite system for the same area. Different acquisition geometry for different orbits should not cause significantly different proportions of objects that create PSs in a particular class. This metric will allow us to compare results obtained with our method with those proposed in other studies.

3.5.2 Qualitative evaluation – 3D visualization

Typically, PSI processing results are visualized in 2D maps as a point with information about the displacement. This type of visualization does not give information about the PS location in 3D space. For instance, PS visualized on a bridge may belong to the bridge deck, bridge support, or another element. By performing 3D visualization, we can more precisely determine from which object or its specific part the PS originates. Regardless of the dimensionality of the visualization, linking PSs to the LiDAR point cloud, as described in the workflow above, leads to new coordinates for numerous PSs. This can pose a challenge in visually verifying the accuracy of the proposed method. Visualizing PS's location before and after linking data, even in 3D, may not give adequate insights if the number of points is very large. In our contribution, we propose another way to visualize the linking results that enable showing PS's original location (P) as well as its corrected location after ICP registration (P′) and the location of the linked LiDAR point (P′′) together with the linking vector (Figure 4). In addition, error ellipsoids are visualized to show the uncertainty of PS locations (Figure 4).

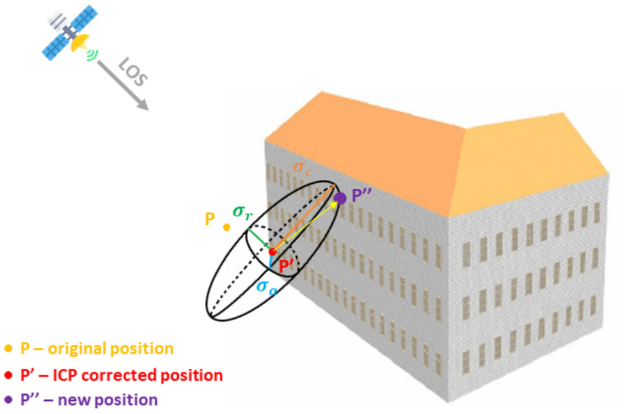

Figure 4: Scheme of 3D visualization of PS-LiDAR linking results for one point. PS point location: original – P (orange), after ICP registration P′ (red), linked LiDAR point P′′ (violet) and the error ellipsoid (black). The shape of the ellipsoid is described by the semi-axes (green, blue, orange) and oriented according to the radar geometry. P′ is the center of the ellipsoid. The linking vector (yellow) to the LiDAR point is within the ellipsoid.

This approach enables visual verification of the linking process and facilitates the interpretation of the PSI results.

The visualization module was also implemented in Python, using packages such as PyVista (https://docs.pyvista.org/) and LasPy (https://laspy.readthedocs.io/). Depending on the analysis, certain visualization elements, such as ellipsoid shapes, vectors, or PSs, may be excluded from the selected stage to improve the interpretation of the results.

4 Data

The presented methodology was applied in two different test sites (Figure 5) – located in Amsterdam, Netherlands (two test fields) and in Ruda Śląska, Poland (one test field). The PSI results were obtained by processing SAR data collected with two satellite systems: C-band Sentinel-1 (S1) and X-band TerraSAR-X (TSX). The PSI processing for each system, depending on available data and to evaluate the efficiency of the proposed algorithm in different scenarios, was executed using data collected from ascending (ASC) and descending (DSC) orbits. The ALS data was obtained from the Polish (geoportal.gov.pl) and Dutch (ahn.nl) national databases. In this study, we used the classification provided by the respective data suppliers. The classification was subjected to a quality check that guaranteed its high accuracy, e.g., total accuracy over 95 % for the Polish dataset. A more detailed description of used datasets is given in Tables 1 and 2 for SAR and ALS data, respectively. By employing multiple ALS and PSI datasets, processed in distinct ways and with varying calculation parameters, we aim to demonstrate the

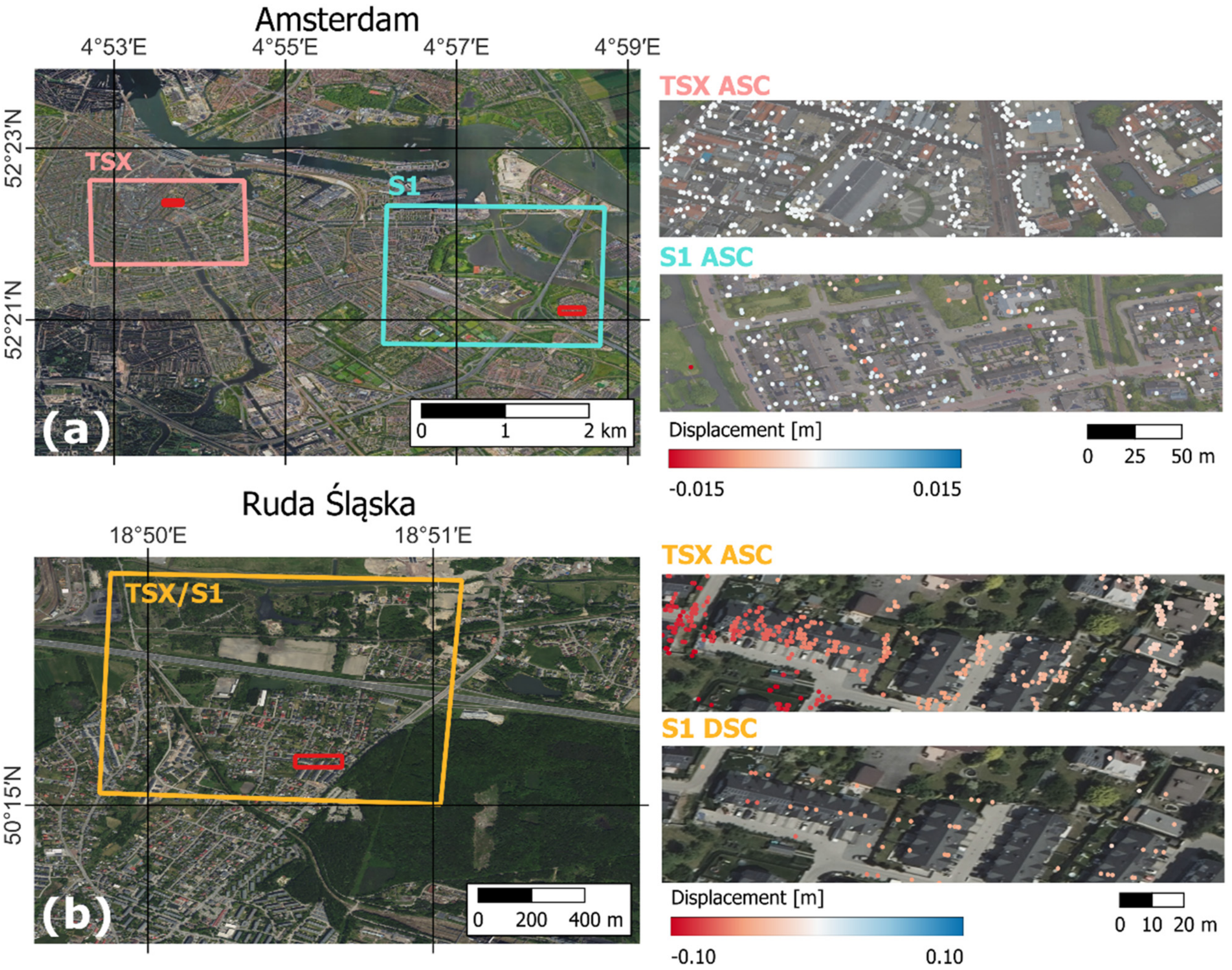

Figure 5: Selected study areas: (a) Amsterdam in the Netherlands and (b) Ruda Śląska in Poland. Pink and cyan rectangles in the Amsterdam study area show the coverage of TerraSAR-X and Sentinel-1 data, respectively. In contrast, the orange rectangle presents the coverage of both TerraSAR-X and Sentinel-1 data in the Ruda Śląska study area. Zoomed views show displacement results obtained through PSI at selected locations marked in red in (a) and (b).

Table 1: Characteristics of the PSI test data.

Test site	Data type		Acquisition period	Number of images	Incidence angle	Azimuth	Point density
Amsterdam	S1	ASC	2015–2019	152	36.04°	349.96°	0.1 pts/m^2
	TSX	ASC	2016–2022	197	30.62°	348.66°	0.2 pts/m^2
	TSX	DSC	2016–2022	196	34.98°	190.72°	0.2 pts/m^2
Ruda Śląska	S1	ASC	2019–2020	51	40.05°	351.81°	0.01 pts/m^2
	S1	DSC	2019–2020	51	33.98°	192.57°	0.01 pts/m^2
	TSX	ASC	2019–2020	25	37.96°	307.96°	0.06 pts/m^2

Table 2: Characteristics of the ALS test data. Numbers of classes according to ASPRS standard [41]. Type of the class according to proposed methodology: I – class completely removed from PS candidate search, II – class completely accepted as PS candidates, III – class requiring additional filtering to search for possible PS candidates, IV – building class requiring filtering to remove points staying in shadow due to SAR acquisition geometry.

Test site	ALS source	Point density	Existing classes:			Acquisition year
			Number and name	Percentage share	Type	
Amsterdam	AHN4 [52]	26 pts/m^2	1 – Unclassified	29 %	III	2019
			2 – Ground	46 %	II	
			6 – Buildings	21 %	IV	
			9 – Water	3 %	I	
			26 – Infrastructure	1 %	II	
Ruda Śląska	GUGiK [53]	19 pts/m^2	0 – Unclassified	3 %	III	2020
			2 – Ground	51 %	II	
			3 – low vegetation	2 %	I	
			4 – medium vegetation	2 %	I	
			5 – high vegetation	13 %	I	
			6 – Buildings	6 %	IV	
			7 – low point	<1 %	I	
			9 – Water	<1 %	I	
			12 – overlap points	23 %	I	

robustness of our method and ensure that the proposed methodology can be applied independently of the input data source.

The first test site is located in the city center of Amsterdam (Figure 5a) and is used to develop and refine the linking method. The SAR data from ascending and both ascending and descending orbits of Sentinel-1 and TerraSAR-X satellites, respectively, were processed using DePSI [11], the PS-InSAR package developed at Delft University of Technology (TU Delft). The density of PS points in the analyzed area varies depending on the satellite mission from which the data originates. For S1 data, this density is about 0.1 pts/m^2, whereas for the same area, the TSX PS density increased to 0.2 pts/m^2, which the spatial resolution of the raw SAR data of these satellite systems can explain. Obviously, PS density is not uniform in the whole area and may differ significantly between different areas due to different land cover. ALS data was obtained free of charge from the fourth AHN (Actueel Hoogtebestand Nederland) campaign, executed in 2020 and named AHN4. This means that objects visible in the LiDAR point cloud are the same as objects visible in TSX data, with a time span of 2016–2022. In the case of S1 data (timespan 2015–2019), the ALS data is slightly younger. Thus, some objects could change. However, it should not impact the linking results as most buildings or infrastructure should be identical in both datasets. The AHN4 point cloud is classified into four classes (numbers and names according to ASPRS standard [41]): Unclassified (class 1), Ground (class 2), Buildings (class 6), Water (class 9), and additional class Infrastructure (class 26). Classes Ground, Building, and Water are homogenous and do not contain other types of objects. However, the Unclassified class contains a mixture of various types of objects such as vegetation, cars, man-made structures, and bridge elements (excluding bridge decks), etc. The AHN4 data also has a special class, number 26, that contains objects such as bridge decks and large road infrastructure, e.g., overhead sign structures. The average AHN4 ALS point cloud density is about 26 pts/m^2.

The second test site was selected to test the method in an area with large ground subsidence. The Polish city Ruda Śląska, located in the Upper Silesia Coal Basin (Figure 5b), was selected for this purpose. This region is known for extensive underground hard coal extraction, resulting in significant terrain surface deformations. PSI products processed with SarScape [54] exhibit lower PS densities than the Amsterdam test site, five and ten times less for S1 and TSX data, respectively. Several reasons can explain it: (1) the occurrence of less compact development and larger areas covered by vegetation, (2) the occurrence of large, fast, and irregularly behaving deformations related to underground mining activities, making it difficult to detect PSs and estimate their displacement time series, (3) different software used for PSI processing, that may impact the number of detected PS points. Both TSX and S1 data were acquired for the same period, i.e., 2019–2020. The Polish ALS point cloud is classified into 9 classes (numbers and names according to ASPRS standard [41]): Unclassified (class 0), Ground (class 2), Low vegetation (class 3), Medium vegetation (class 4), High vegetation (class 5), Buildings (class 6), Low points (class 7), Water (class 9), and Overlap points (class 12). Similarly to the previous test site, not all classes contain homogeneous elements. Class 0 (Unclassified) includes all points that do not belong to other classes and contain elements such as poles, cars, fences, power lines, structural elements of bridges, and elements of small road infrastructure. Classes related to vegetation (class 3–5) were distinguished based on vegetation height above ground level. Class 12 contains all points collected from cross-strips in the dataset but did not cover the test site. In the case of ALS data, the point cloud density for the Ruda Śląska test site equals 19 pts/m^2, slightly lower than for the Amsterdam test site.

5 Results

5.1 PS position uncertainties

The standard PSI approach was used with two software programs to obtain PS displacements in the presented areas of interest: DePSI and SarScape were employed for the Amsterdam and Ruda Śląska test sites, respectively. Based on accuracy metrics provided during PSI processing, we estimated each PS's position uncertainty in range, azimuth, and cross-range directions. Figure 6 presents boxplots of the obtained uncertainty in each dimension for both case studies and the different SAR datasets.

The major uncertainty was encountered in both sites for S1 PSI products. The larger is directly related to the pixel spacing of the SAR data, which is 2.3 m × 14.1 m and 1.5 m × 1.8 m for the S1 and TSX missions, respectively, in the range and azimuth directions. The mean uncertainties for S1 in Amsterdam, where DePSI software for PSI calculations was used are 0.9 m, 5.4 m, and 4.4 m for range, azimuth, and cross-range, respectively, and correspond to the results presented in ref. [50]. If we compare solutions from two different software, it is clearly visible that the uncertainty values, as well as their variations, are lower for the DePSI solution (Figure 6a–c) than for SarScape (Figure 6d–f). It should be highlighted that DePSI calculates the coordinates of points in the radar coordinate system as sub-pixel positions, while SarScape lacks this capability, which will significantly impact the obtained results. The results confirmed the need to improve the accuracy of PS localization with other methods apart from the standard PSI technique processing, as described in the following sections of this paper.

5.2 LiDAR point cloud processing results

During the initial PS candidate selection stage, any LiDAR points with return numbers greater than 1 were removed. Then geometric parameters such as planarity, linearity, and normal vectors were estimated based on PCA (see Figure 2). Classes with suitable candidates for linking were found for the Dutch ALS dataset from the Ground (class 2), Building (class 6), Infrastructure (class 26), and Unclassified (class 1) classes. For the Polish ALS dataset, the infrastructure class was not specifically identified, resulting in the selection of solely the Ground (class 2), Building (class 6), and Unclassified (class 0) classes. It is important to note that the Dutch point cloud lacks the vegetation class, unlike the Polish ALS point cloud, causing more challenges in searching for man-made structures in the Unclassified class. Geometrical filtering in class 1 (Dutch dataset) or 0 (Polish dataset) is based on the planarity or linearity values. The test that was executed on optimal hyperparameter selection resulted in the radius of the local neighborhood being equal to 2 m, planarity threshold $S = 0.7$, and linearity threshold $L = 0.6$ for both ALS datasets. Datasets with similar characteristics, especially point cloud densities, are expected to result in similar values of the above hyperparameters. However, for point clouds with notably higher or lower densities and accuracies (e.g., those obtained through different techniques), experimental verification of radius, planarity, and linearity values should be executed. Figure 7 presents the quantitative results of ALS point cloud filtering for ICP registration and further linking with the Sentinel-1 ascending dataset (removed points are marked with hatches). According to the proposed workflow, the filtering applied for selecting potential PS candidates reduced the ALS point clouds to 51 % and

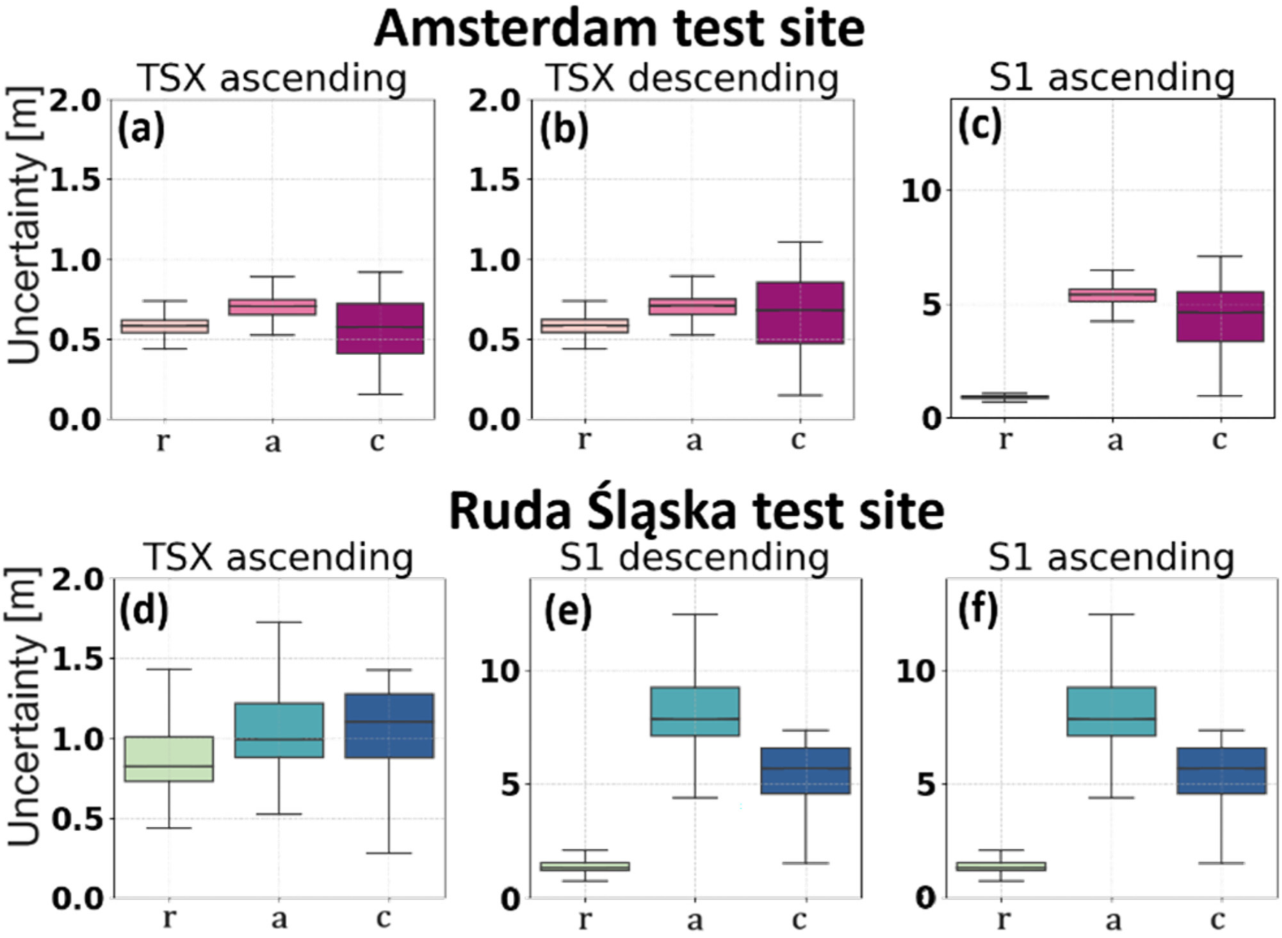

Figure 6: Uncertainties of the PS point positions in r – range, a – azimuth and c – cross–range for the Amsterdam (a–c) and Ruda Śląska (d–f) test sites.

46 % (Figure 7, sum of green values) of their original sizes for the Amsterdam and Ruda Śląska datasets, respectively. Depending on the geometry of the SAR data with which the ALS point cloud is linked, this value changes because the number of points rejected from the Buildings class due to SAR geometry varies. These differences range between 1 and 2 %.

The results of filtering the Unclassified class were added to a new class – Other (marked in solid gray in Figure 7). Depending on the area of interest, it contained 0.03 % and 1 % of all ALS points for Amsterdam and Ruda Śląska datasets, respectively. Thanks to filtering based on geometrical features, it was possible to find suitable PS linking candidates in the Unclassified class and belonging to linear objects (Figure 8a), road barriers, or structural elements of bridges (Figure 8b). Additionally, it incorporated points from flat surfaces, specifically some misclassified building points, enabling them for further analysis and linking.

Considering the selection of possible candidates based on their position in relation to the acquisition geometry, we determined the angles between the LiDAR normal vectors and the PS LOS vector Figure 9 presents the results for selection based on the TSX ascending (Figure 9b) and descending (Figure 9c) geometry for the same building. This approach makes it possible to reject LiDAR points obscured by other points (Figure 9b) from further analysis.

5.3 PS global transformation results

The next step is the estimation of global transformation parameters for the PSs. The ICP algorithm was adopted to calculate global transformation parameters between PS and LiDAR point clouds. The LiDAR point cloud, which contains only points after PS linking candidate selection (Section 3.2), was chosen as the reference cloud. Utilizing the transformation obtained from the ICP method with the Open3D library, the effectiveness of this process is assessed using two

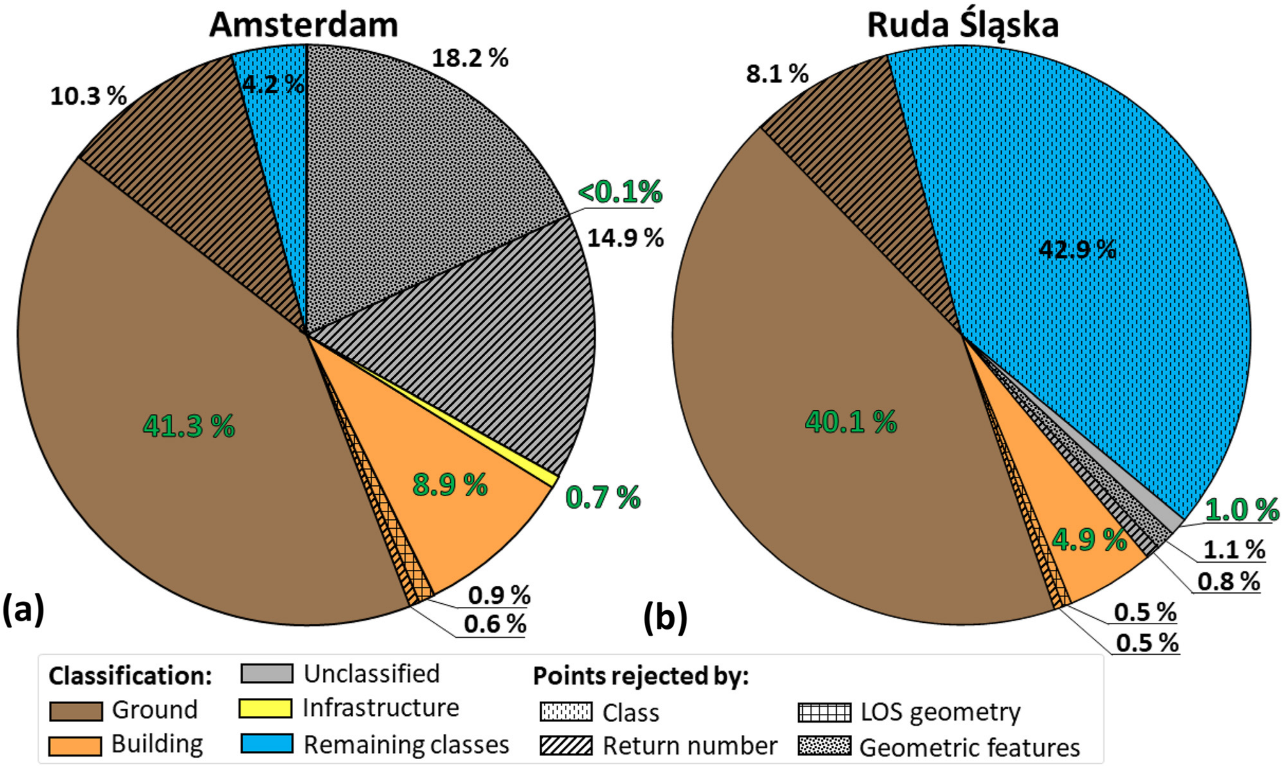

Figure 7: Filtering results of ALS point clouds for linking with ascending Sentinel-1 mission data: (a) Amsterdam, (b) Ruda Śląska. The pie charts illustrate point classes and the filtering process applied to ALS point clouds: (1) colors represent individual classes existing in ALS data. (2) Hatches indicate points removed at each filtering stage based on specific criteria, including class-based filtering, return number filtering, LOS geometry filtering, and geometric feature filtering. (3) Labels show the point percentages of each part of pie chart relative to the total number of points in the dataset; green labels indicate percentages of points used for the final PS-ALS linking, while black labels indicate percentage of points removed during filtering.

metrics, including point fitness, describing the percentage of PSs that are inliers, and RMSE, determining the accuracy of alignment through the root mean square error for correctly matched points. RMSE is calculated based on point-to-plane distances for inlier points. Global transformation parameters and ICP registration performance measures are listed in Table 3.

Despite the significant difference in density between the ALS and PS point clouds, the ICP algorithm found correspondences to 78.1 %–98.3 % PSs in the LiDAR point cloud that met the point-to-plane maximal distance criteria. Obviously, these correspondences are not necessarily linking points (P″) (Figure 4) since they may be outside the ellipsoid error. The S1 data showed over 90 % matching for both case studies, potentially due to the higher acceptable search radius. Considering the obtained RMSE values presented in Table 3, it can be observed that for the TSX data sets the value is much lower and is about 0.9 m, while for S1 it is between 3.4 and 4.1 m, which is also coincident with the spatial resolution of S1 and TSX data. The process of determining global parameters using ICP was successful. The transformation parameters were determined based on over 75 % of all PSs, and the average distances between them (based on RMSE) are smaller than the resolution of SAR images.

For all analyzed datasets, the transformation primarily involves translation, with the rotation angles being close to 0. The determined translation parameter values are higher for Sentinel-1 data, that can be attributed to the lower PS position accuracy estimated during processing (Figure 6). Additionally, the highest values are observed in the vertical component (Tz). For the TSX datasets, the difference between the translations for the horizontal (Tx, Ty) and vertical components is much lower. When the transformation parameters were calculated, the point cloud of the PSs was transformed, resulting in their corrected localization (P′) (Figure 4).

5.4 Final linking – results validation

The final linking procedure for PS within the 2-sigma confidence level ellipsoid was conducted in two study areas

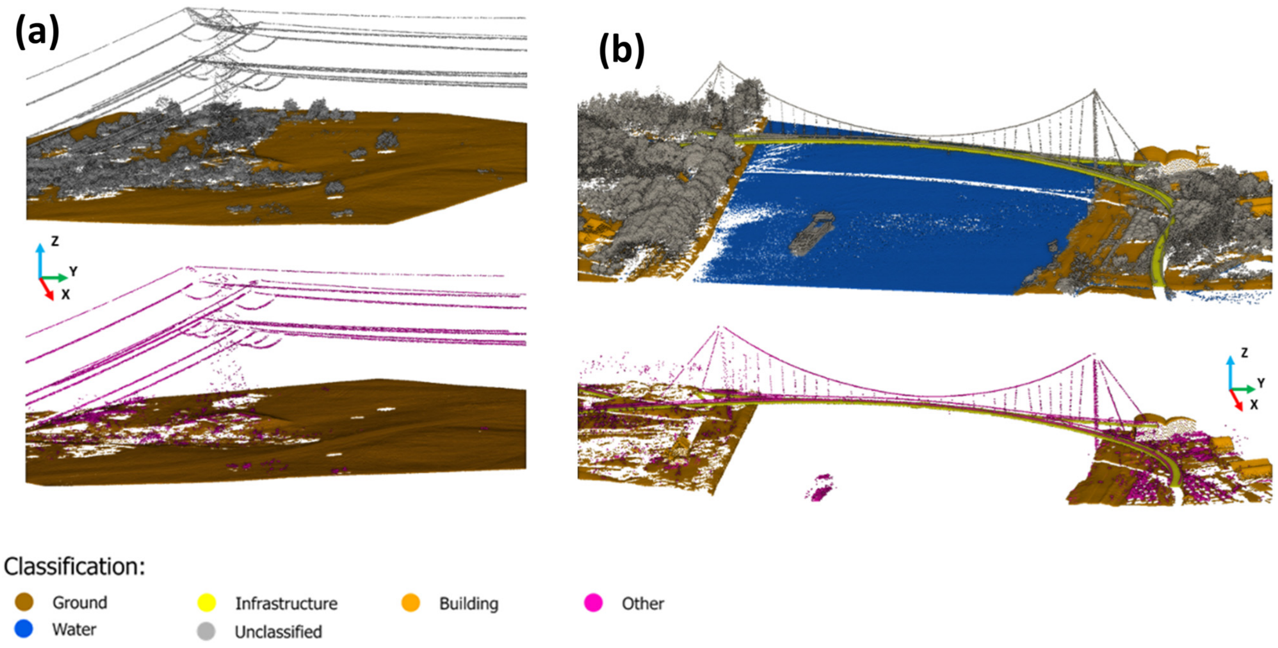

Figure 8: Examples of the Dutch LiDAR point cloud before (top) and after (bottom) PS candidate filtering. Colors mean point classes: grey – class 1 (unclassified), brown – class 2 (ground), orange – class 6 (building), blue – class 8 (water), yellow – class 26 infrastructure), pink – class 27 (other). (a) Power line mast and surroundings. (b) Bridge and surroundings.

for points with corrected localization (P′, Figure 4): Amsterdam and Ruda Śląska, using three datasets for each location. The obtained linking results, categorized into individual point classes according to the ALS data classification, as a percentage distribution is depicted in Figure 10a. In addition, the results obtained for processing, excluding one of two key steps of the proposed method, are also included. Figure 10b shows linking percentages for processing without systematic error removal by applying global transformation using parameters determined with the ICP algorithm (Section 3.3), and Figure 10c shows linking percentages for processing without ALS point cloud filtering (Section 3.2).

Thanks to the proposed approach, 80 % of the PS points from the Sentinel-1 ascending orbit and 72 % and 71 % of the PS from TerraSAR-X ascending and descending orbits, respectively, were linked to real objects in the Amsterdam case study (Figure 10a). The results were comparable for the Ruda Śląska case study, with 88 %, 90 %, and 65 % linked PSs determined from the Sentinel-1 descending, Sentinel-1

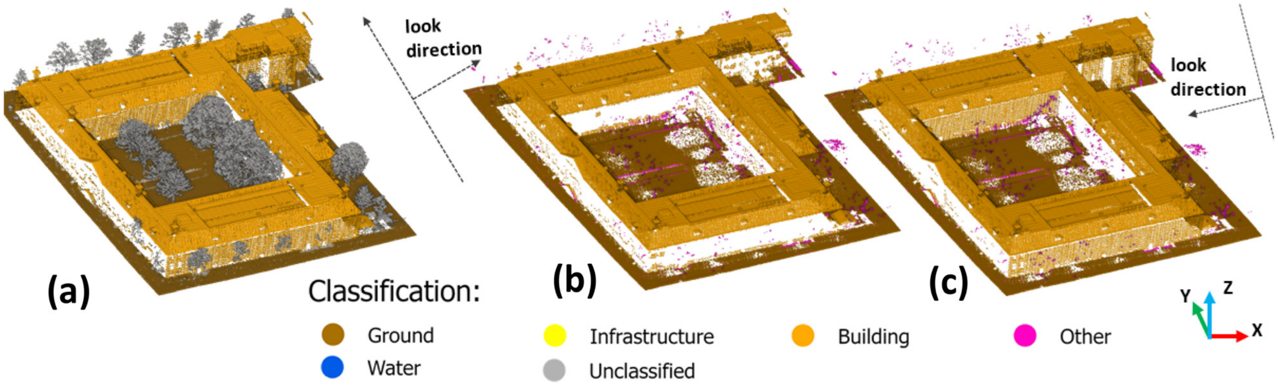

Figure 9: Example of building in Dutch LiDAR point cloud before (a) and after PS candidate filtering depending on the LOS direction for ascending (b) and descending (c) orbit. Colors mean point classes: grey – class 1 (unclassified), brown – class 2 (ground), orange – class 6 (building), blue – class 8 (water), yellow – class 26 (infrastructure), pink – class 27 (other).

Table 3: Transformation parameters obtained using ICP for Amsterdam and Ruda Śląska. Tx, Ty, and Tz represent translation, while φ, θ, ψ denote Euler rotation angles. Point fitness and RMSE indicate ICP registration performance.

Test site	Dataset	Translation [m]			Rotation [deg]			Point fitness [%]	RMSE [m]
		Tx	Ty	Tz	φ	θ	ψ		
Amsterdam	S1 ASC	0.561	3.150	6.783	−0.006	0.042	−0.007	98.3	4.089
	TSX DSC	−1.264	−1.354	0.121	0.002	−0.005	0.005	88.5	0.856
	TSX ASC	0.458	−1.319	−0.161	0.013	−0.023	0.001	82.2	0.837
Ruda Śląska	S1 DSC	5.142	−3.196	7.202	0.463	0.218	−0.361	93.2	3.403
	S1 ASC	−7.981	−0.025	−8.005	0.194	−0.025	0.379	94.5	3.587
	TSX DSC	−4.919	0.343	3.753	−0.071	0.032	−0.071	78.1	0.927

ascending, and TerraSAR-X ascending orbits, respectively (Figure 10a).

The percentage distribution between different classes varied depending on the analyzed study area. For Amsterdam, the area analyzed is located in the city's center, where high-density housing occurs. For the Ruda Śląska area, single-family housing dominates. In addition, there is a highway crossing the Ruda Śląska test site, and points are classified as Ground, making this class the majority of linked PS (50 %). Additionally, the Other class (Figure 10a) was extracted from the Unclassified class utilizing PCA planarity and linearity features. It contains linking points for infrastructure objects, such as high-voltage poles (Figure 11a), thus increasing the percentage of linked PSs. This is particularly true for Sentinel-1 data, where the percentages of the Other class for Amsterdam are 19 % (S1 ASC), 8 % (S1 DSC), and 9 % (S1 ASC) for Ruda Ślaska.

The results of processing that excludes one of the processing steps (Figure 10b and c) demonstrate that systematic bias removal by utilizing ICP for the estimation of global transformation parameters is a crucial step. Omitting the global transformation executed with ICP leads to a decrease in the percentage of linked points in all case studies, except for the Sentinel-1 dataset in Amsterdam, where a slight increase of 1 % is observed. However, in this case, the proportion of points linked to the building and ground classes changes (Figure 10b). Moreover, the execution of global transformation also ensures that the percentages of PSs assigned to each class are similar for both DSC and ASCdatasets of the same SAR system. For example, without the global transformation step, in the S1 ASC and S1 DSC datasets for Ruda Śląska, a notable discrepancy existed in the number of PSs classified for each class, e.g., 34 % and 61 % for Ground class for ASC and DSC datasets, respectively (Figure 10b). Applying global transformation using parameters estimated with ICP allowed for balancing these proportions, e.g., 51 % and 56 % for the Ground class for ASC and DSC datasets, respectively (Figure 10a). This reflects better the fact that both datasets represent the same area and product, while small differences occur due to differences in LOS geometry. Moreover, for the S1 DSC dataset for Ruda Śląska, the positive value of vertical translation (Table 3) corrected misclassifications of PSs (initially below the terrain), linking them correctly to buildings instead of incorrectly to the ground (compare percentages for Buildings and Ground classes in Figure 10a and b, Ruda Śląska S1 DSC). In contrast, for the ASC dataset, where PSs were initially above the terrain, causing that most of them to be linked to buildings (Figure 10b, Ruda Śląska S1 ASC), the global transformation allowed to improve their linkage to ground points (Figure 10a, Ruda Śląska S1 ASC). The global transformation utilizing ICP effectively mitigated systematic errors, enhancing the reliability and accuracy of the linking process.

ALS data filtering step was similarly vital for improving linking accuracy. Filtering reduces the likelihood of linking PSs to classes unlikely to generate persistent scatterers, such as vegetation, water, or unclassified objects, e.g., vehicles or temporary structures (Figure 10c, green and grey bars). While skipping this step increases the overall percentage of linked points, it results in decreased linking quality, with PSs more frequently misclassified.

The quality of the lining process may be asses also by the distribution of the linking vector lengths between the corrected PS (P′, Figure 4) and the linked PS (P″, Figure 4). Histograms of linking vector lengths (Figure 12) demonstrate that the magnitude of the vectors corresponds well to the data resolution. The 3D vector lengths mostly do not exceed 2 m for TSX and 10 m for S1 in both case studies.

Despite the higher initial accuracy in positioning PS for TerraSAR-X data (Figure 6), finally, fewer percentage of points were linked to real objects compared to Sentinel-1 data (Figure 10a). This is particularly evident in the case of the Upper Silesia region. Visual analysis of the obtained

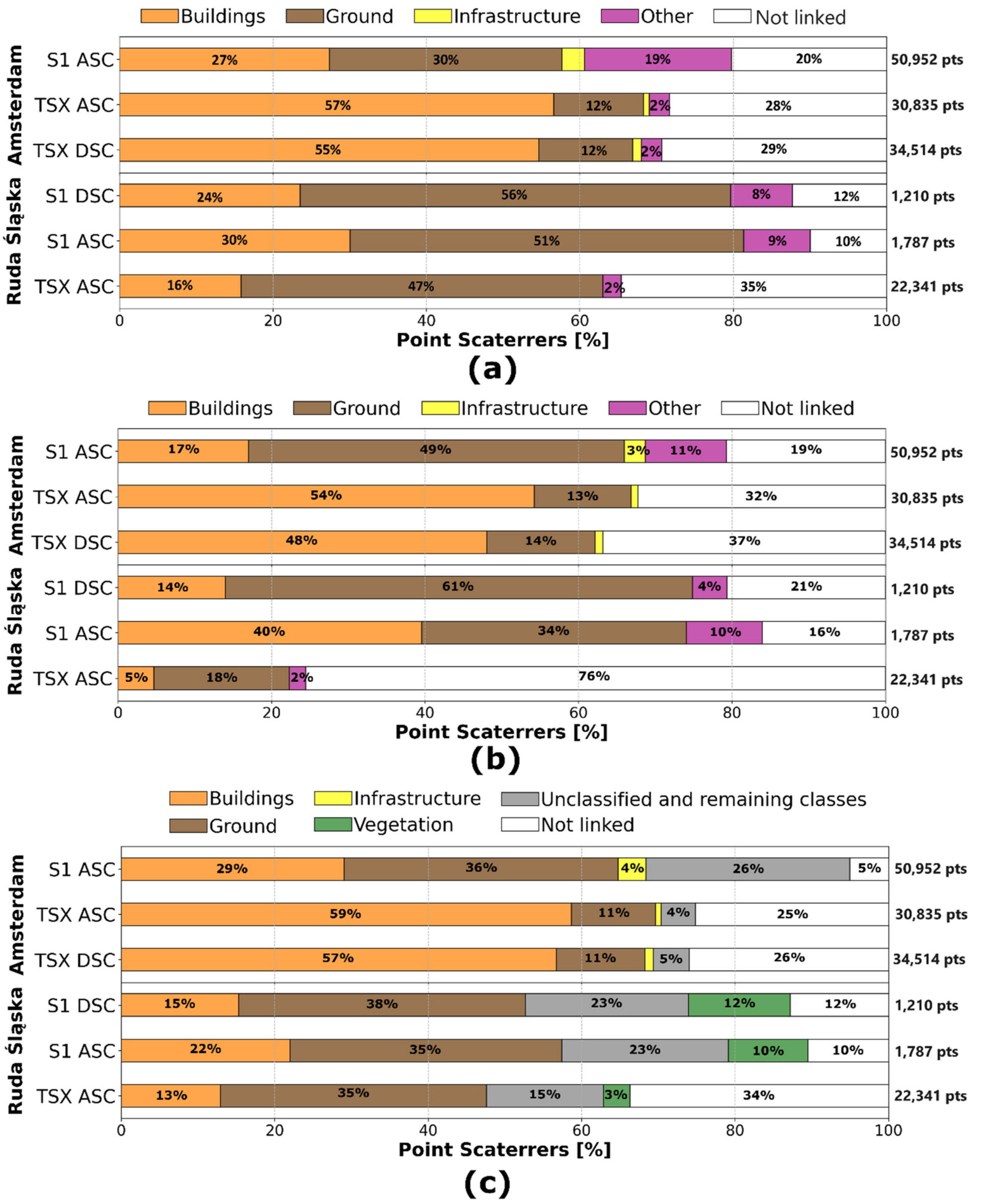

Figure 10: Percentage of linked PSs categorized into point classes according to the ALS data classification and PSs that could not be linked: (a) according to the proposed method, (b) excluding global transformation utilizing ICP, (c) excluding ALS data filtering. The infrastructure class is limited to the ALS dataset from Amsterdam, where it is labeled.

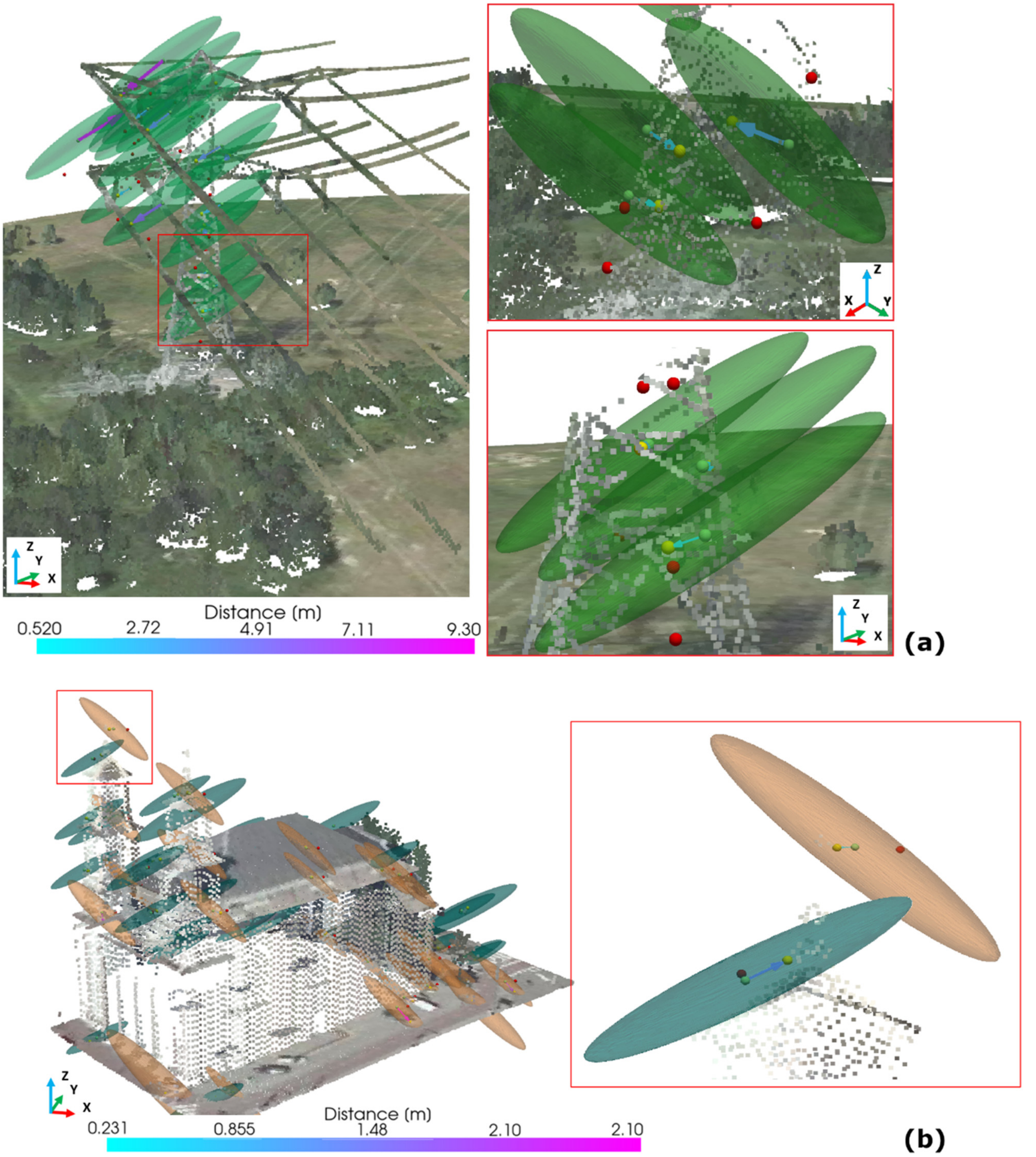

Figure 11: Linking results for selected objects: (a) high-voltage pole and S1 ASC PSs with error ellipsoids (green) for each point – Amsterdam test site, (b) TSX PS linking results with error ellipsoids for each point from both ASC (green ellipsoids) and DSC (orange ellipsoids) orbits – Amsterdam test site. PSs colors: original – red, after ICP registration – green, linked with LiDAR – yellow. The arrows connect the points after the ICP with the linked position, and their color describes the distance between the points.

results reveals that the positioning of PS from TerraSAR-X often occurs near the vertical walls of buildings (Figure 13, green dots). One of the key factors contributing to the observed difference in linking percentages between S1 and TSX is the limitation of ALS data, particularly its scan geometry. Gaps in the ALS data frequently occur on building

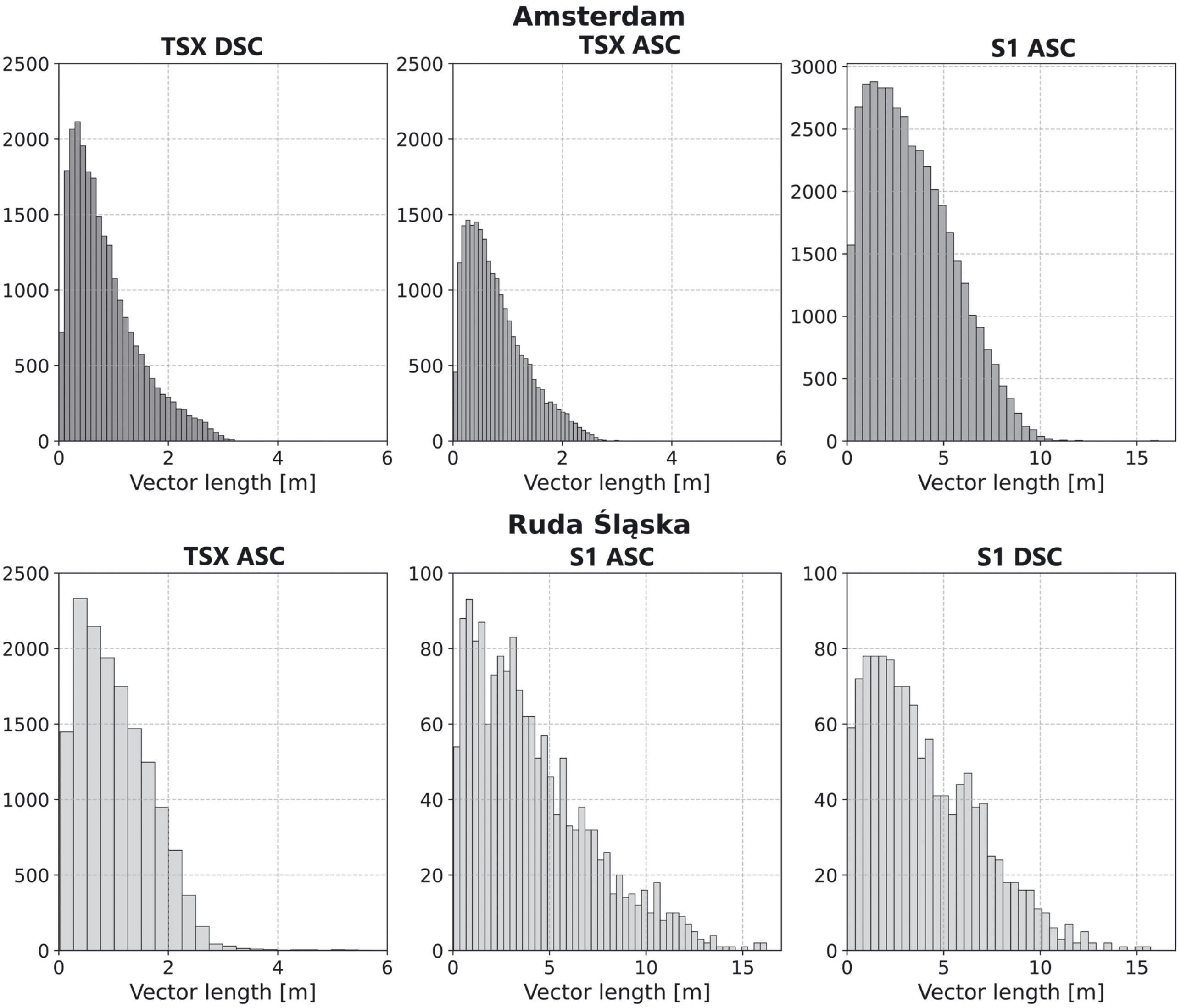

Figure 12: Histograms of the linking vectors (P′P″) for both TSX and S1 datasets in Amsterdam (top row) and Ruda Ślaska (bottom row), respectively.

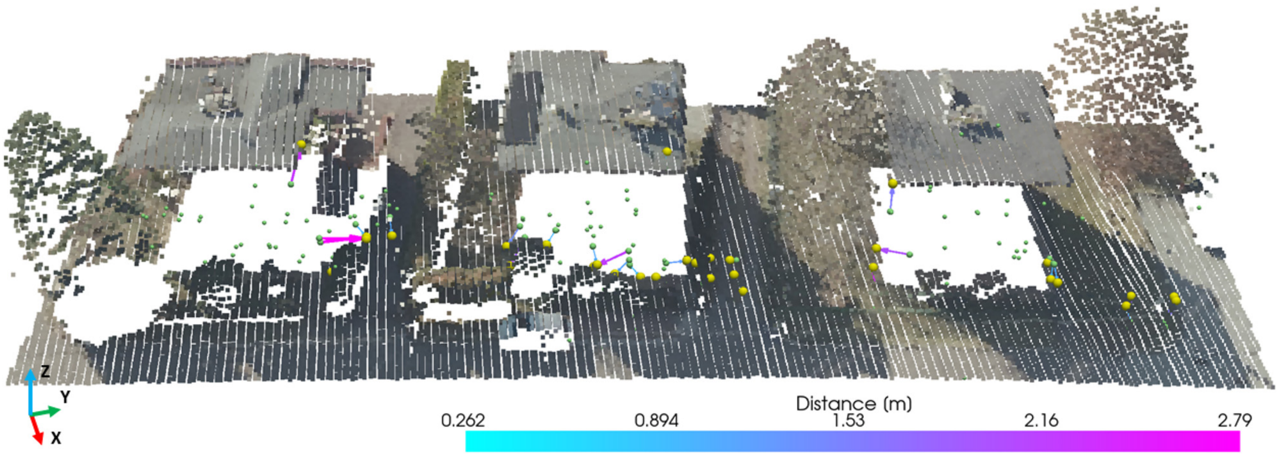

Figure 13: Example of buildings with missing LiDAR points on the walls in Ruda Śląska test site. The green color indicates PSs obtained from TSX ASC orbit before linking (P′), and the yellow color indicates linked LiDAR point (P″). Arrows connect the new positions of the points, and their color describes the distance between them.

walls or in shadows, especially in densely built-up areas, as clearly shown in Figure 13. When PSs form near buildings, a double-bounce reflection often occurs, i.e., wall-ground reflections, where the actual PS position lies at the intersection of these two surfaces. Since these vertical surfaces are typically absent from ALS data, the correct links cannot be created. For individual buildings, TSX, due to its higher data resolution compared to Sentinel-1, often generates more points corresponding to building facades. As a result, fewer percentage of points are linked in these areas, making it more challenging to establish reliable correspondences. The smaller positional uncertainty of TSX PSs, represented by their error ellipsoids, restricts the spatial area within which a match can be identified. Conversely, the larger positional uncertainty of Sentinel-1 PSs facilitates linkage, as the broader error ellipsoid increases the likelihood of finding a match within the available ALS data. The absence of links to PSs located on walls supports the validity of the proposed method. It was designed to identify only reliable links rather than to maximize their number, which would lead to numerous erroneous links.

6 Discussion

Our research presented a method for linking PS to real objects mapped with the ALS point cloud. The study utilized various forms of data, including radar (both ascending and descending geometries, as well as radar missions utilizing X-band and C-band wavelengths) and point clouds (varied density and classification schemes), acquired for different land uses (Amsterdam city center, a segment of highway, and single-family houses in Ruda Śląska), to fully investigate the flexibility of the proposed approach. Based on a chosen PS confidence threshold of 2-sigma, the percentage of linked PSs was equal to 80 %, 72 %, and 71 % for the Sentinel-1 ascending, TerraSAR-X ascending, and descending orbits, respectively, in the Amsterdam area. Similarly, in Ruda Śląska, 88 %, 90 %, and 65 % PSs were linked for Sentinel-1 ascending, descending, and TerraSAR-X ascending data. The achieved results demonstrate consistency in the links found within a single dataset (S1, TSX), regardless of the orbit.

The results compared with other case studies presented previously show a similar level of correlation. However, it is difficult to compare the results directly because each work analyzed data for a different area, for which the distribution of both PS and ALS data will be different. In ref. [22] authors achieved 80 % linked PS obtained from TerraSAR-X data. In contrast [50], reported that 98 % of the PSs from Sentinel-1 were associated with the real object. The significant number of observed connections is mainly due to the specific and limited size of the area of interest, which is the railway line. Our considerations focused on areas that are different in terms of land use. In addition to linking points to real objects, in our method, PSs have gained an additional attribute based on the linked LiDAR point classification, which is very valuable, especially in further analysis, as it allows filtering the data on the determined displacements and better evaluating them.

Previous research focused solely on the selection of assigned classes, like Ground or Buildings [29, 31], or analysis of the entire dataset, which is assumed to result in erroneous geo-located PS due to linking to LiDAR points with classes such as vegetation or water bodies [50]. In contrast, our method considers additional objects extracted from unclassified points, mainly road and urban infrastructure elements, which provide a stable radar signal reflection. The methodology applied enabled the identification of links for between 3 % and 19 % of the additional PSs in this point group, depending on the area analyzed, thereby confirming the validity of the selected filtering. In the candidate selection, their positioning relative to the satellite viewing geometry was considered, minimizing the likelihood of linking PSs to LiDAR points in shadow with respect to the SAR sensor. Considering the radar viewing geometry is a crucial step that particularly benefits in estimating global transformation parameters. The ICP algorithm was utilized for this purpose (Section 3.3). The results obtained show that using the ICP algorithm, the PS cloud can be preliminarily aligned with the ALS point cloud. Transformations are mainly translation, rotation parameters (φ, θ, ψ) are very small (Table 3). Depending on the type of satellite mission, the size of the shift varies and is directly related to the initial position accuracy, which is much better for the X-band (TSX) than the C-band (S1).

Performing a 3D visualization concept, which includes LiDAR data and PS position from each step of processing, together with error ellipsoids, enables result interpretation in relation to radar signal direction as well as scene geometry. Visualization of the linking vector helps further to interpret the direction of movement of the new position. The standard nearest neighbor approach does not take the scattering mechanism into account, which means that the result of the linking is not always the real center of the dominant scattering object. Including information about the direction of linking vectors enables the verification of the validity of the PS link to a specific object in space. Moreover, the 3D visualization made it possible to identify some limitations of the approach used. Primarily, the ALS point cloud sometimes contains gaps that result in the PSs not being linked to LiDAR points or being linked to points in the error ellipsoids that correspond to a different part of the building or even a completely different object. The lack of links is particularly noticeable for TSX data, which usually results in more PSs due to the better spatial resolution of X-band data. Connections to the wrong part of the object or another structure are much more common for S1 data. Here, the error ellipsoid is larger than for TSX, which increases the probability of connecting to more distant points. It can be reduced by integrating ALS with additional point clouds from other techniques: MLS, TLS, ULS, or point clouds created from images using dense image matching.

Nonetheless, this method enables the correlation of the precise displacement data with probable source locations. Although exact identification of the PS source is not achievable, linking information is sufficient to perform detailed displacement analyses, even in the context of changes within a single object. In addition, assigning a class based on the point cloud will allow analyses to consider types of displacement specific to a class of objects, e.g., the thermal signal for bridges caused by temperature changes.

7 Conclusions

The proposed approach improved the localization of PSs, which was shown by the large number of PSs whose confidence ellipsoids contained potential scattering points represented in the ALS dataset. Using this method, more than 80 % and 65 % of the PSs derived from PSI processing of Sentinel-1 and TerraSAR-X mission data, respectively, were linked to real-world objects regardless of the orbit geometry. The proposed method is able to achieve this by introducing two novel elements: treating the PSs as point clouds, which allowed their global transformation using ICP, and preselecting the LiDAR points that could be PSs using simple filters. To the best of the authors' knowledge, this approach has not been utilized before. Although the tools used are well-known, they have not been utilized in this manner.

We introduce a method for preliminary filtering of LiDAR point clouds to enhance ICP registration reliability and select candidates for linking with PSs. This method analyzes available classes in the point cloud, return number, and geometric features such as planarity, linearity, and normal vectors calculated using PCA. This filtering process enables the extraction of points associated with objects that efficiently reflect radar waves, thus forming stable scatterers. The tests have demonstrated the universality of the method, indicating its applicability to a variety of PSI products: different imaging geometries, satellite missions, software; and ALS data: different sensors, point cloud densities, classification methods, as well as areas with diverse land use. However, it is essential to possess prior knowledge regarding the content of objects within individual classes. This information is crucial for determining the classes for which the proposed selection step should be implemented. Applying the ICP algorithm on selected points is crucial to minimize systematic shifts between data sets, which helps with the final linking. Using a 3D visualization module is essential for verifying the methodology, helping to understand the results, and effectively controlling the entire process. The limitation of this method is the appropriate ALS dataset. ALS data on a nationwide scale are mainly collected for topographic purposes (i.e., for the construction of Digital Surface Models – DSMs or Digital Terrain Models – DTMs). Due to the nature of these data, vertical surfaces such as building walls are often missing points. To get a more complete mapping, the best solution would be to use a scanner with a different scanning mechanism (e.g. Palmer scanner), or to use point clouds from other sources (e.g. point cloud from dense image matching).

Acknowledgments: The presented investigation was accomplished as part of a scientific internship at Delft University of Technology (TU Delft), Netherlands, conducted within the GATHERS project, funded by the European Union's Horizon 2020 research and innovation program under grant agreement No 857612.

This work was supported by the Wrocław University of Environmental and Life Sciences (Poland) as the Ph.D. research program „Bon doktoranta SD UPWr" from the subsidy increased by the minister responsible for higher education and science for the period 2020–2026 in the amount of 2 % of the subsidy referred to Art. 387 (3) of the Act of 20 July 2018 – Law on Higher Education and Science, obtained in 2019. The authors would like to thank German Aerospace Center (DLR) for providing X-band data over the study area within the project GEO3759.

Research ethics: Not applicable.

Informed consent: Not applicable.

Author contributions: NW: Conceptualization, Methodology, Software, Validation, Formal analysis, Investigation, Writing – Original Draft, Review & Editing. **GJ**: Conceptualization, Methodology, Validation, Writing – Original Draft, Review & Editing. **FvL**: Conceptualization, Methodology, Data Curation Writing – Review & Editing. **RH**: Conceptualization, Writing – Review & Editing. **KPF**: Data Curation, Writing – Review & Editing. All authors have accepted responsibility for the entire content of this manuscript and approved its submission.

Use of Large Language Models, AI and Machine Learning Tools: None declared.

Conflict of interest: The authors state no conflict of interest.

Research funding: GATHERS project, funded by the European Union's Horizon 2020 research and innovation program under grant agreement No 857612. Wrocław University of Environmental and Life Sciences (Poland) as the Ph.D. research program „Bon doktoranta SD UPWr" from the subsidy increased by the minister responsible for higher education and science for the period 2020–2026 in the amount of 2 % of the subsidy referred to Art. 387 (3) of the Act of 20 July 2018 – Law on Higher Education and Science, obtained in 2019.
Data availability: Not applicable.

References

1. Ferretti A, Prati C, Rocca F. Permanent scatterers in SAR interferometry. IEEE Trans Geosci Rem Sens 2001;39:8—20.
2. Crosetto M, Monserrat O, Cuevas-González M, Devanthéry N, Crippa B. Persistent scatterer interferometry: a review. ISPRS J Photogrammetry Remote Sens 2016;115:78—89.
3. Ramzan U, Fan H, Aeman H, Ali M, AA Al-qaness M. Combined analysis of PS-InSAR and hypsometry integral (HI) for comparing seismic vulnerability and assessment of various regions of Pakistan. Sci Rep 2022;12:22423.
4. Ciampalini A, Bardi F, Bianchini S, Frodella W, Del Ventisette C, Moretti S, et al. Analysis of building deformation in landslide area using multisensor PSInSARTM technique. Int J Appl Earth Obs Geoinf 2014;33:166—80.
5. Di Martire D, Paci M, Confuorto P, Costabile S, Guastaferro F, Verta A, et al. A nation-wide system for landslide mapping and risk management in Italy: the second not-ordinary plan of environmental remote sensing. Int J Appl Earth Obs Geoinf 2017;63:143—57.
6. Hooper A, Segall P, Zebker H. Persistent scatterer interferometric synthetic aperture radar for crustal deformation analysis, with application to Volcán Alcedo. Galápagos J Geophys Res Solid Earth 2007;112. https://doi.org/10.1029/2006JB004763.
7. Ramirez RA, Lee GJ, Choi SK, Kwon TH, Kim YC, Ryu HH, et al. Monitoring of construction-induced urban ground deformations using Sentinel-1 PS-InSAR: the case study of tunneling in Dangjin, Korea. Int J Appl Earth Obs Geoinf 2022;108:102721.
8. Zhang B, Liao X, Zhang J, Xiong S, Wang C, Wu S, et al. Megalopolitan-scale ground deformation along metro lines in the Guangdong-Hong Kong-Macao Greater Bay Area, China, revealed by MT-InSAR. Int J Appl Earth Obs Geoinf 2023;122:103432.
9. Pawluszek-Filipiak K, Borkowski A. Monitoring mining-induced subsidence by integrating differential radar interferometry and persistent scatterer techniques. Eur J Remote Sens 2021;54:18—30.
10. Modeste G, Doubre C, Masson F. Time evolution of mining-related residual subsidence monitored over a 24-year period using InSAR in southern Alsace, France. Int J Appl Earth Obs Geoinf 2021;102:102392.
11. Van Leijen F. Persistent scatterer interferometry based on geodetic estimation theory [Ph.D. thesis]. Delft University of Technology; 2014.
12. Omidalizarandi M, Mohammadivojdan B, Alkhatib H, Paffenholz J-A, Neumann I. On the quality checking of persistent scatterer interferometry data by spatial-temporal modelling. J Appl Geodesy 2023;17:119—31.
13. Nefros C, Alatza S, Loupasakis C, Kontoes C. Persistent scatterer interferometry (PSI) technique for the identification and monitoring of critical landslide areas in a regional and mountainous road network. Remote Sens 2023;15:1550.
14. Huang Q, Crosetto M, Monserrat O, Crippa B. Displacement monitoring and modelling of a high-speed railway bridge using C-band Sentinel-1 data. ISPRS J Photogrammetry Remote Sens 2017;128:204—11.
15. Jung J, Kim D, Palanisamy Vadivel SK, Yun SH. Long-term deflection monitoring for bridges using X and C-band time-series SAR interferometry. Remote Sens 2019;11:1258.
16. Gernhardt S, Bamler R. Deformation monitoring of single buildings using meter-resolution SAR data in PSI. ISPRS J Photogrammetry Remote Sens 2012;73:68—79.
17. Crosetto M, Solari L, Balasis-Levinsen J, Casagli N, Frei M, Oyen A, et al. Ground deformation monitoring at continental scale: the European ground motion service. Int Arch Photogram Rem Sens Spatial Inf Sci 2020;43:293—8.
18. Yang M, Dheenathayalan P, López-Dekker P, van Leijen F, Liao M, Hanssen RF. On the influence of sub-pixel position correction for PS localization accuracy and time series quality. ISPRS J Photogrammetry Remote Sens 2020;165:98—107.
19. Yang M, Wang R, Li M, Liao M. A PSI targets characterization approach to interpreting surface displacement signals: a case study of the Shanghai metro tunnels. Remote Sens Environ 2022;280:113150.
20. Zhu XX, Montazeri S, Ali M, Hua Y, Wang Y, Mou L, et al. Deep learning meets SAR: concepts, models, pitfalls, and perspectives. IEEE Geosci Remote Sens Mag 2021;9:143—72.
21. Milillo P, Sacco G, Di Martire D, Hua H. Neural network pattern recognition experiments toward a fully automatic detection of anomalies in InSAR time series of surface deformation. Front Earth Sci 2022;9:728643.
22. Van Natijne AL, Lindenbergh RC, Hanssen RF. Massive linking of PS-InSAR deformations to a national airborne laser point cloud. Int Arch Photogramm Remote Sens Spatial Inf Sci-ISPRS Archives 2018;42:1137—44.
23. Dheenathayalan P, Small D, Schubert A, Hanssen RF. High-precision positioning of radar scatterers. J Geod 2016;90:403—22.
24. Eineder M, Minet C, Steigenberger P, Cong X, Fritz T. Imaging geodesy — toward centimeter-level ranging accuracy with TerraSAR-X. IEEE Trans Geosci Rem Sens 2010;49:661—71.
25. Cong X, Balss U, Eineder M, Fritz T. Imaging geodesy — centimeter-level ranging accuracy with TerraSAR-X: an update. IEEE Geosci Remote Sens Lett 2012;9:948—52.
26. Schubert A, Small D, Miranda N, Geudtner D, Meier E. Sentinel-1A product geolocation accuracy: commissioning phase results. Remote Sens 2015;7:9431—49.
27. Montazeri S, Rodríguez González F, Zhu XX. Geocoding error correction for InSAR point clouds. Remote Sens 2018;10:1523.
28. Yang M, López-Dekker P, Dheenathayalan P, Liao M, Hanssen RF. On the value of corner reflectors and surface models in InSAR

precise point positioning. ISPRS J Photogrammetry Remote Sens 2019;158:113−22.

29. Hu F, van Leijen FJ, Chang L, Wu J, Hanssen RF. Monitoring deformation along railway systems combining multi-temporal InSAR and LiDAR data. Remote Sens 2019;11:2298.
30. Yang M, López-Dekker P, Dheenathayalan P, Biljecki F, Liao M, Hanssen RF. Linking persistent scatterers to the built environment using Ray tracing on urban models. IEEE Trans Geosci Rem Sens 2019;57:5764−76.
31. Schneider PJ, Soergel U. Matching persistent scatterer clusters to building elements in mesh representation. ISPRS Ann Photogramm Remote Sens Spat Inf Sci 2022;V-3-2022: 123−30.
32. Vitale S, Ferraioli G, Pascazio V, Schirinzi G. InSAR-MONet: interferometric SAR phase denoising using a multiobjective neural network. IEEE Trans Geosci Rem Sens 2022;60:1−14.
33. Yang Y, Chen B, Li Z, Yu C, Song C, Guo F. A novel phase unwrapping method for low coherence interferograms in coal mining areas based on a fully convolutional neural network. IEEE J Sel Top Appl Earth Obs Rem Sens 2024;17:601−13.
34. Harris CR, Millman KJ, van der Walt SJ, Gommers R, Virtanen P, Cournapeau D, et al. Array programming with NumPy. Nature 2020;585:357−62.
35. Cigna F, Esquivel Ramirez R, Tapete D. Accuracy of sentinel-1 PSI and SBAS InSAR displacement velocities against GNSS and geodetic leveling monitoring data. Remote Sens 2021;13: 4800.
36. Zhang Y, Zhang J, Wu H, Lu Z, Guangtong S. Monitoring of urban subsidence with SAR interferometric point target analysis: a case study in Suzhou, China. Int J Appl Earth Obs Geoinf 2011;13: 812−8.
37. Ho Tong Minh D, Hanssen R, Rocca F. Radar interferometry: 20 years of development in time series techniques and future perspectives. Remote Sens 2020;12:1364.
38. Sousa JJ, Hooper AJ, Hanssen RF, Bastos LC, Ruiz AM. Persistent Scatterer InSAR: a comparison of methodologies based on a model of temporal deformation vs. spatial correlation selection criteria. Remote Sens Environ 2011;115:2652−63.
39. Baarda W. S-transformations and criterion matrices. Delft, The Netherlands: Netherlands Geodetic Commission; 1973.
40. Schunert A, Soergel U. Assignment of persistent scatterers to buildings. IEEE Trans Geosci Rem Sens 2016;54:3116−27.
41. ASPRS LAS Specification. https://github.com/ASPRSorg/LAS [Accessed 21 Aug 2024].
42. Thiel KH, Wehr A. Performance capabilities of laser scanners−an overview and measurement principle analysis. Int Arch Photogram Rem Sens Spatial Inf Sci 2004;36:14−8.
43. Demantké J, Mallet C, David N, Vallet B. Dimensionality based scale selection in 3D lidar point clouds. Int Arch Photogram Rem Sens Spatial Inf Sci 2012;38:97−102.
44. Weinmann M, Jutzi B, Hinz S, Mallet C. Semantic point cloud interpretation based on optimal neighborhoods, relevant features and efficient classifiers. ISPRS J Photogrammetry Remote Sens 2015;105:286−304.
45. Lehtomäki M, Kukko A, Matikainen L, Hyyppä J, Kaartinen H, Jaakkola A. Power line mapping technique using all-terrain mobile laser scanning. Autom ConStruct 2019;105:102802.
46. Zhou QY, Park J, Koltun V. Open3D: a modern library for 3D data processing. ArXiv Preprint ArXiv:180109847; 2018.
47. Glira P, Pfeifer N, Briese C, Ressl C. A correspondence framework for ALS strip adjustments based on variants of the ICP algorithm. PFG Photogramm Fernerkundung Geoinf 2015;2015:275−89.
48. Hyvärinen A, Hurri J, Hoyer PO, Hyvärinen A, Hurri J, Hoyer PO. Principal components and whitening. Nat Image Stat Probab Approach Early Comput Vis 2009:93−130. https://doi.org/10.1007/978-1-84882-491-1_5.
49. Dheenathayalan P, Small D, Hanssen RF. 3-D positioning and target association for medium-resolution SAR sensors. IEEE Trans Geosci Rem Sens 2018;56:6841−53.
50. Chang L, Sakpal NP, Elberink SO, Wang H. Railway infrastructure classification and instability identification using Sentinel-1 SAR and laser scanning data. Sensors 2020;20:7108.
51. He Y, Xu G, Kaufmann H, Wang J, Ma H, Liu T. Integration of InSAR and LiDAR technologies for a detailed urban subsidence and hazard assessment in Shenzhen, China. Remote Sens 2021;13:2366.
52. ahn.nl. https://www.ahn.nl/ [Accessed 29 Aug 2024].
53. geoportal.gov.pl. https://mapy.geoportal.gov.pl/imap/ [Accessed 29 Aug 2024].
54. Sarmap SA. Synthetic aperture radar and SARscape: SAR guidebook. Purasca, Switzerland: Sarmap SA; 2009:274 p.